ALMA MATER STUDIORUM · UNIVERSITÀ DI BOLOGNA

Scuola di Scienze
Corso di Laurea Magistrale in Fisica

Electrical Spectroscopy of Rubrene Bulk and Thin Film Crystals

Relatore:
Prof.ssa Beatrice Fraboni

Correlatore:
Dott. Andrea Ciavatti

Presentata da:
Silvia Grande

Sessione III
Anno Accademico 2012/2013

Abstract

One of the most diffused electronic device is the field effect transistor (FET), contained in number of billions in each electronic device. Organic optoelectronics is an emerging field that exploits the unique properties of conjugated organic materials to develop new applications that require a combination of performance, low cost and processability. Organic single crystals are the material with best performances and purity among the variety of different form of organic semiconductors. This thesis is focused on electrical and optical characterization of Rubrene single crystal bulk and thin films. Rubrene bulk is well known but for the first time we studied thin films. The first Current-voltage characterization has been performed for the first time on three Rubrene thin films with three different thickness to extract the charge carriers mobility and to assess its crystalline structure. As results we see that mobility increase with thickness. Field effect transistor based on Rubrene thin films on SiO_2 have been characterize by current-voltage (I-V) analyses (at several temperatures) and reveals a hopping conduction. Hopping behavior probably is due to the lattice mismatch with the substrate or intrinsic defectivity of the thin films. To understand effects of contact resistance we tested thin films with the Transmission Line Method (TLM) method. The TLM method revealeds that contact resistance is negligible but evidenced a Schottky behavior in a limited but well determined range of T. To avoid this effect we carried out annealing treatment after the electrode evaporation iswe performed a compete I-V characterization as a function of in temperature to extract the electronic density of states (DOS) distribution through the Space Charge Limited Current (SCLC) method. The results show a DOS with an exponential trenddistribution, as expected. The measured mobility of thin films is about $0.1 cm^2/Vs$ and it increases with the film thickness. Further studies are necessary to investigate the reason and improve performances. From photocurrent spectrum we calculated an Eg of about 2.2eV and both thin films and bulk have a good crystal order. Further measurement are necessary to solve some open problems.

Uno dei dispositivi più diffusi in elettrona è il field effect transistor. Ogni dispositivo elettronico ne contiene miliardi. L'elettronica a base organica è un campo emergente che riesce a sfruttare le proprietà uniche dei mteriali organici quali: basso costo, resa e facilità di processo. I cristalli organici sono materiali con le prestazioni maggiori e alto grado di purezza fra tutte le tipologie presenti di semionduttori organici. Questa tesi si concentra sullz caratterizzazione elettrica ed ottica del Rubrene cristallino, sia bulk che film sottile. Il rubrene in forma buljkè bene conosciuto e studiato da diversi anni , i film sottili rappresentano una novità. Abbiamo effettuato misure di tensione-corrente su film sottili di diverso spessore così da poter calcolare la mobilità ed evidenziare l'ordine cristallino in funzione dello spessore. Il field effect transistor costituito da Rubrene a film sottile depositato su uno strato di ossido di silicio (SiO_2) è stato caratterizzato elettricamente al variare della temperatura rivelanso una conduzione di tipo hopping. Questo comportamento, probabilmente, è dovuto a problemi di interfaccia fra il reticolo cristallino del rubrene e quello dell'ossido si silicio., oppure a difetti strutturali interni del film. Abbiamo, inoltre, studiato gli effetti della resistenza di contatto tramite il metodo Transmission Line Model (TLM), fra in contatti in oro ed il semiconduttore, al variare della temepratura. Queste misure hanno mostrato che la reisistenza di contatto è effettivamente trascurabile ma, inaspettatamente, abbiamo notato un comportamento da diodo Schottky in un bene determinato range di temperature. Per eliminare questo effetto abbiamo scaldato i campioni (processo di annealing) a 60° er circa 10 minuti e ripetuto la caratterizzazione IV a diverse T. Effettivamente la barriera Schttky non era più presente. Da queste misure abbiamo ricavanto anche la densità degli stati di trappole utilizzando la teoria Space-Charge-Limited Current (SCLC). I risultati mostrano una distribuzione esponenziale di stati, così come previsto dalla teoria. La mobilità misurata nei nostri film sottili è circa $0.1 cm^2/Vs$ ed aumenta all'aumentare dello spessore del film. Ulteriori studi sono ancora da effettuare per capire totalmente le ragioni di questo comportamento e migliorarne le prestazioni. Infine, abbiamo effettuato misure di fotocorretente per avere un quadro il più completo possibile circa le caratteristiche dei nostri campioni. Dagli spettri di fotocorrente abbiamo estratto l'ampiezza dell'energia di gap pari a $2.2 eV$ circa. Stesso valore sia per i film sottili che per il bulk, è una riprova del buon grado di cristallinità dei campioni. Per risolvere diversi quesiti ancora in cerca di risposta occorrono ulteriri misure.

Contents

Introduction **9**

1 Rubrene: physical properties **11**
1.1 Introduction . . . 11
1.2 Rubrene's Molecule . . . 11
1.2.1 Crystalline Rubrene . . . 12
1.3 Effects of oxidation on rubrene crystal . . . 13
1.4 Growth of rubrene thin films . . . 14
1.5 Transport properties of crystalline rubrene . . . 15

2 Experimental Setup **19**
2.1 IV Measurement Setup . . . 19
2.2 Rubrene Sample . . . 21
2.3 Basic Concepts of a Field Effect Transistor . . . 22
2.4 Photocurrent setup . . . 25

3 Basic principles of SCLC **27**
3.1 Indroduction . . . 27
3.2 Trap free insulator . . . 27
3.2.1 Geurst law for thin films . . . 28
3.3 Correction to perfect trap free insulator . . . 29
3.4 Differential Method of SCLC . . . 31
3.5 Temperature modulated SCLC . . . 32
3.6 The density of States (DOS) . . . 35
3.7 Cubic spline deconvolution method . . . 36
3.8 Relevant Energy Levels . . . 37
3.9 Space-Charge-limited currents in organic films: Some open problems . . . 38

4 Experimental Results **41**
4.1 Introduction . . . 41
4.2 Rubrene bulk . . . 42
4.3 Rubrene thin films . . . 43
4.4 Rubrene Field Effect Transistor . . . 47

4.4.1 Mobility . . . 53
4.4.2 Contact Resistance Effects . . . 54
4.4.3 Contact Resistance results . . . 56
4.4.4 Annealed thin film IV characteristic . . . 60

5 Photocurrent **65**
5.1 Experimental Results . . . 69
5.1.1 Photocurrent on rubrene bulk and thin films . . . 73

Conclusions and Outlook **80**

Bibliography **83**

Introduction

The electronic properties of organic single crystals have been intensively studied forThe electronic properties of organic single crystals have been intensively studied forover 40 years. Recent reports indicate that, organic single-crystal field-effect transistors have generated results that are comparable in performance to hydrogenated amorphous silicon. Organic thin-film transistors are being actively used for a wide area of electronic applications, but their mobilities are limited by structural imperfections and impurities.

Organic single crystals, on the other hand, have been limited to charge-transport studies mainly because the fabrication of single-crystal transistors poses a technological challenge. The main resources of organic semiconductors are their low cost, availability, light weight, versatilities and flexibility.

The factors that determine the quality of an organic transistor are the mobility of the charge carriers, the device stability, its operating voltage and the ratio between the intensity of the current in the on and off states. All these parameters, combined with the necessity of low-cost production, drive the search for new active material or the improvements of already existing ones. In the latter case much effort remains to be made to fully understand the properties of the interfaces, which are the sources of most non-ideal effects that limit the performances of the devices. At the present time, the best performance registered for an organic transistor has been obtained with Rubrene single crystals. Also, using a single crystal allows to better analyze the influence of defects and impurities on the device characteristics. Rubrene $(C_{42}H_{28})$ belongs to the group of polycyclic aromatic hydrocarbons builtd with four benzene rings placed side by side each other. Rubrene is a well studied molecule, the great innovation of this work is the employment of thin films to fabricate a field effect transistor. We analyzed rubrene single crystal thin films and bulk. On crystallinethin films of rubrenecrystal we collected IV characteristic in a wide range of temperatures to extract mobility and the electronic density of states distribution using the SCLC model. After this characterization we focused our attention on field effect transistor (FET) fabricated with of rubrene thin film upon silicon oxide. From FET's IV characterization results we decided to investigate the effects of contact resistance on device using TLM method TLM analysis, performed at varying temperatures,shownevidenced a Schottky behavior in a temperature range from 190 to 280K. To avoid this Schottky effect we carried out an annealing process to improve the electrodes injecting properties and repeated IV characteristic. Finally we performed photocurrent analyses on the same samples (bulk and thin films) usto assess the value of energy gap and to confirm the good crystal order of thin films.

Chapter 1

Rubrene: physical properties

1.1 Introduction

Rubrene (5,6,11,12-Tetraphenyltetracene, $C_{42}H_{28}$) is one of the best performing organic single crystal semiconductors for electronic device application. At the same time it's still presenting some open problems which limits its performances, as its chemical instability in the presence of oxygen, the difficult to obtain a good crystalline quality samples and its efficiency not optimized yet. In this chapter we illustrate rubrene physical and chemical structure correlated with transport properties.

1.2 Rubrene's Molecule

Rubrene belongs to the group of polycyclic aromatic hydrocarbons and consist of a tetracene backbone (it's build with four benzene rings placed side by side each other), with a phenyl ring bonded on each side of the two centralbenzene rings, as shown in figure 1.1.

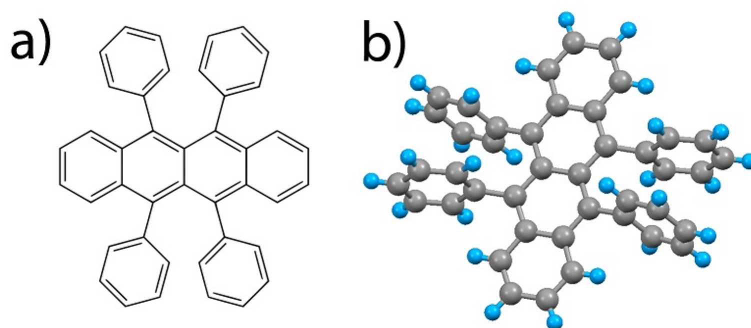

Figure 1.1: Structural formula (a) and three-dimensional sketch (b) of a rubrene molecule

Rubrene molecules tend to oxidize when exposed to air, light strongly enhances this process. [1]. An oxidized rubrene molecular becomes a rubrene peroxide and experiments show that the most common form of peroxide formed after oxidation is the endoperoxide

[2][3], in which molecular oxygen is lined to one of the two central rings of the tetracene backbone as shown in a following figure).

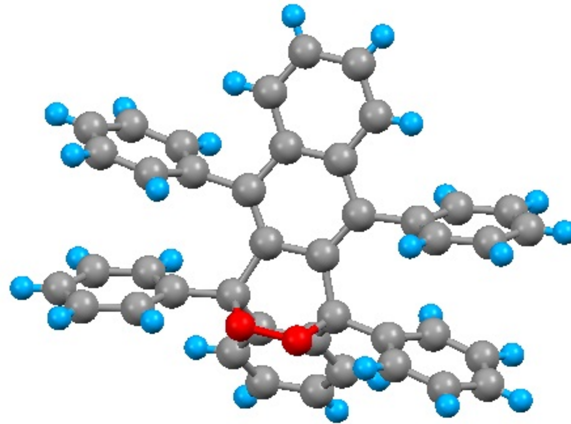

Figure 1.2: Three-dimensional sketch of a rubrene endoperoxide molecule. In red oxigen atoms

The bonding with oxygen generate a deformation of the molecular organization, this causes a break of the π molecular orbital. This contamination affects optical properties of crystal, at a first look rubrene solution and amorphous film became transparent from their original reddish color.

1.2.1 Crystalline Rubrene

One of the most important achievement reached with Rubrene is its crystalline structure which improves enormously is potential in electronic applications, thanks to its electrical parameters and efficiency.

To obtain that form we have to follow several step and a particular growth processing.

The way used to create crystals influence their final structure and consequently their response to physical input. The molecular arrangement in the three main known rubrene polymorphs are monoclinic, triclinic and orthorhombic. In fig 1.3 is shown the three kind of lattice in which it's possible an arrangement of rubrene molecules. Looking at the three structure from a direction normal with respect to the long axis of molecules, it's possible identify the amount of $\pi - \pi$ stacking between the conjugate backbones of adjacent molecules.

Operatively, monoclinic and triclinic lattice structure can be obtained by solution crystallization methods [4] , while the third unit cell, orthorhombic, needs physical vapor deposition to be formed [4].

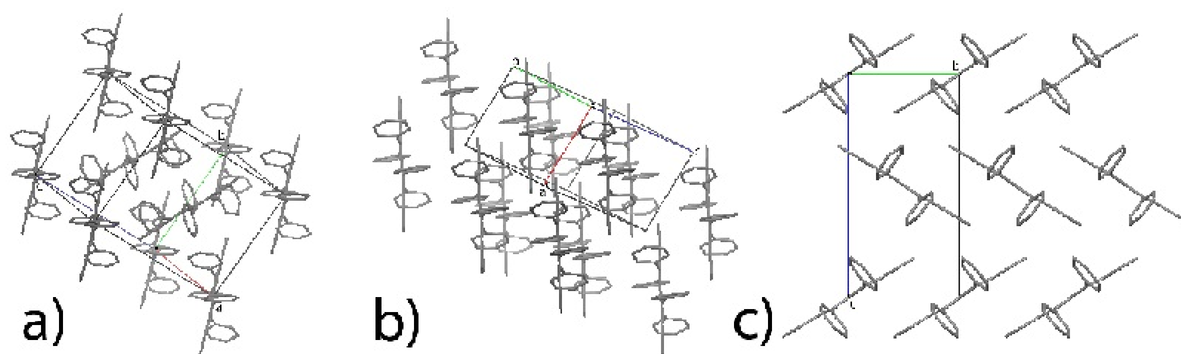

Figure 1.3: Arrangement of molecules in the three known rubrene polymorphs: monoclinic (a), triclinic (b), orthorhombic (c). The strucures are observed in a direction normal with respect to long axis of the molecules, in order to easly show the amount of $\pi - \pi$ stacking between adjacent molecules.

In the fig.1.3 we can see that:

- In the monoclinic polymorph the molecular planes of two neighbor molecules are almost normal to each other, thus yielding no $\pi - \pi$ stacking at all;
- in the triclinic polymorph the molecular planes of adjacent molecules are all parallel but also laterally shifted with respect to each other, leading only to a partial superposition of their π orbitals in the stacking direction;
- at last configuration, orthorhombic polymorph the molecules are arranged in the herringbone packing, with an almost complete $\pi - \pi$ stacking in the b lattice direction.

It can be noticed that along the **a** axes the molecule is stacked in a single layer interacting only with through their phenyl rings. This induces an important anisotropy in the intermolecular interactions in the perpendicular plane (b, c) with respect to those in the **a** direction of lattice. It influences the growth dynamics of the crystal.

1.3 Effects of oxidation on rubrene crystal

As mentioned above, Rubrene is strongly affected by oxidation. This effect plays an important role to understand electrical and optical transport in whole crystal. Oxygen is not the only impurity within the rubrene sample, also we have other contaminants which are incorporated during crystal growth ; rubrene peroxide has been shown to be the dominant impurity in commercial rubrene powder and the presence of small amounts of oxygen in the inert gas flow used for crystal growth has been show to increase the amount of such impurities in the crystals [5][6]. In order to improve material quality a deal may be a purification of the source material through several sublimation cycle and a carefully controlled growth environment.

A very interesting analysis is a study of oxidation after the growth process, when a complete rubrene crystal stays exposed in air for several days. This study was performed by [3]

through a spectrometer mass.

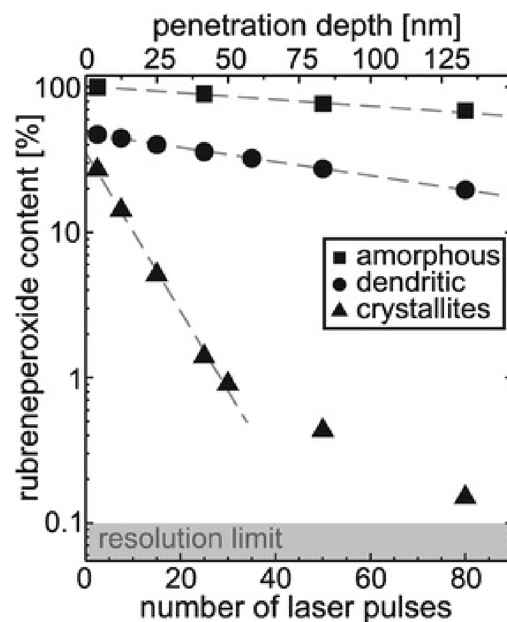

Figure 1.4: Depth profiles of rubrene peroxide concentration in rubrene thin film with different degree of crystallinity as determined bt mass spctroscopy. From [3]

In a fig.1.4 is shown the concentration of rubrene peroxide molecules in rubrene thin films of different crystalline quality as a function of depth is reported. It's easy to see in amorphous or dendritic film the amount of peroxide is larger and in a deeper layers than rubrene crystallites which present a minus absolute quantities and only in a the first layers. A possible reason is that in rubrene crystals the staking contrast the oxygen penetration, but not totally. The role of rubrene peroxide in the transport properties of rubrene single crystals is also still subject to debate. In chapter 3 we will examine photocurrent theory and in chapter 6 will report results and possible effect of oxidation.

Najafov et al. in [7] have shown that in organic single crystals exposed to light photoconductivity present a not negligible decrease correlated to the increase oxygen exposure time.

1.4 Growth of rubrene thin films

Why a thin film? Because it is the better configuration to study the intrinsic properties of a material. Easy and rapid to growth in a reproducible way and with an high structural quality. In order to further to employ rubrene in electronic devices, it is necessary to minimize device dimension and then their components. Moreover, the large anisotropy in the optical and electrical properties requires a high control over the crystalline form of the thin films, the goal is to obtain a monocrystalline rubrene thin film.

In order to achieve this goal, the method of epitaxial growth on other inorganic substrates such as Au or Bi or on organic single crystal like tetracene has been employed. Other method like evaporation or solution lead to amorphous films [8][9].
Epitaxial thin films of high quality can be grown by Organic Molecular Beam Epitaxy (OMBE), an evolution of Molecular Beam Epitaxy (MBE). This technique consists in slowly depositing the sublimated molecules on the desired substrate in an ultra high vacuum (UHV) atmosphere. In this way is possible to grow sample with thickness down to a fraction of a single layer, further it is possible monitor each of atomic layer deposited and have a total control of entire process. In fig **??** is shown a generic MBE apparatus. The system consist

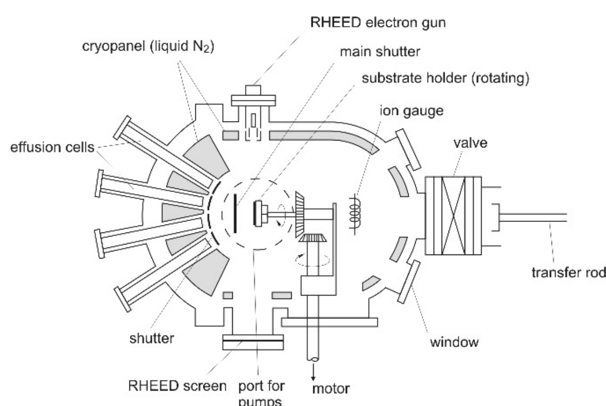

Figure 1.5: MBE apparatus scheme

of an introduction and transfer chamber, used to insert the clean substrate and to extract the sample after the deposition, and of the deposition chamber. A gate valves divided two chambers to keep deposition chamber alway in UHV and minimizing external contaminations. A system of three pumps guarantees ultra high vacuum regime: rotative, turbomolecular and a cryopump. Inside the deposition chamber there are several crucible which contain desired material in a powder form then sublimated with an heating wire. The deposition rate and the nominal thickness of the deposited film are monitored with a quartz microbalance sitting aside the substrate.

During deposition process is also possible to control the temperature of the sample . Finally, the structural evolution of the film during the deposition can be monitored by a *reflectance anisotropy spectroscopy* (RAS) system, an in situ characterization technique based on the real- time monitoring of the reflectance anisotropy of the sample surface during the deposition [10]. Through TEM, AFM and X-ray spectroscopy our samples have been thoroughly characterized.

1.5 Transport properties of crystalline rubrene

Interest toward rubrene is motivated by its good electrical transport properties. As for most organic crystals , electrical transport in crystalline rubrene is strongly anisotropic, with the larger mobility values measured along the **b** lattice direction. rubrene, like most organic

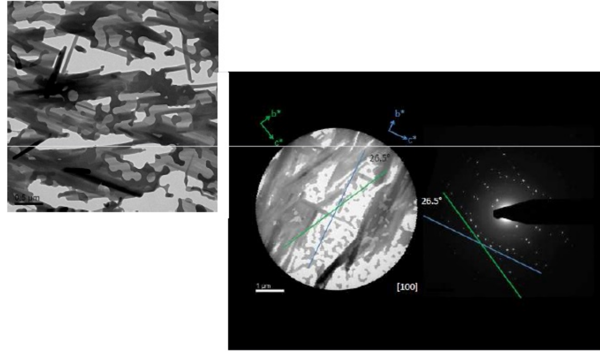

Figure 1.6: TEM (ETH Zurich) image of a rubrene thin film sample with nominal thickness 15nm

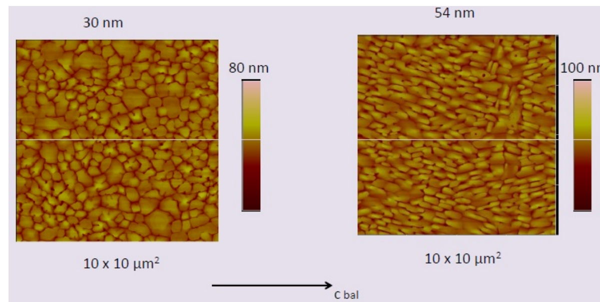

Figure 1.7: AFM image of rubrene thin film

semiconductors, is also a unipolar p-type material, holes give high value of mobility while electron mobility is several orders of magnitude smaller.

In organic Molecular Crystals (OMC) the intermolecular interaction forces are weak Van der Waals type processes with a binding energy of around $10^{-3} - 10^{-2}$eV. Therefore the electronic structure of the single molecules is nearly conserved, which leads the tendency of localization of charge carriers on individual molecules of the crystal. The self-energy of charge carrier in OMC is determined by many-electron effects (polarization) and can be described by a single-electron approach. In case of rubrene is possible to consider small molecules with conjugated bonds. This system consist of alternating double bonds and single bonds. The wave function of π electrons lie in the molecular plane generating an overlapping of wave functions, if overlap is large the π electrons are delocalized along the whole molecules. $\pi - \pi$ stacking corresponds direction of maximum conduction (**b** axes).

The crucial parameter is the intermolecular transfer integral that describes the ease of transfer of a charge between two adjacent molecules. Molecular interaction creates an equivalent of energy gap of an inorganic semiconductor. The highest occupied energy level is called HOMO (highest occupied molecular orbital) and lowest empty energy level is LUMO (lowest unoccupied molecular orbital).

For pure single crystals band-like transport was observed down to low temperatures [11], as in inorganic semiconductors. In this case the total widths and the shapes of the valence

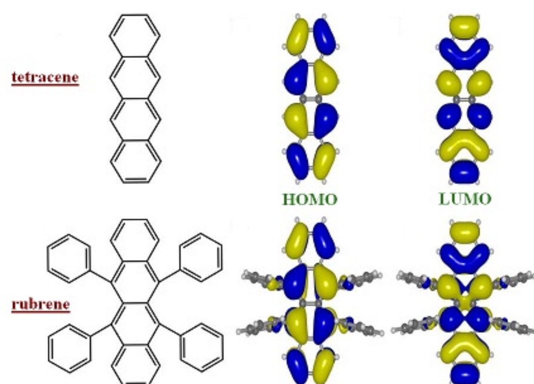

Figure 1.8: Rapresentation of HOMO and LUMO for tetracene and rubrene. The sign is represented by the colors

and conduction band determine the hole and electron mobilities. With increasing temperature the electron-phonon coupling leads to a strong enhancement of localization of the charge carrier and the transport mechanism changes to phonon-assisted hopping. This interchanging between band-like and hopping transport was first described by Holstein [12]. Holstein model predicts that a low temperature the bands are broad and increasing temperature they become more narrow in agreement with interaction between band transport and phonon assisted hopping. In this work is omitted explicit calculation of model. Also is found that electron-phonon coupling decrease with increasing molecular size .

In organic molecular crystals electrical transport is usually determined by the capture of the involved charge carriers in localized states. These trap states are energetically placed in the energy gap (among HOMO and LUMO). Traps states may be induced by imperfections of the crystal structure or chemical impurities introduced to the lattice.

Chapter 2

Experimental Setup

2.1 IV Measurement Setup

To perform current-voltage measurement was used two different setup. The first one to operate in air and the second in vacuum. Operating at room temperature and in air we have Keithley (2614a or 6514 electrometer) as source-meter, probe station and an optical microscopy to prepare sample and place the probes. According to the type of sample and measurement we choose right Keithley model and configuration. To characterize a field effect transistor we need two source-meter, one for drain-source voltage and the second for gate voltage connected as in figure:

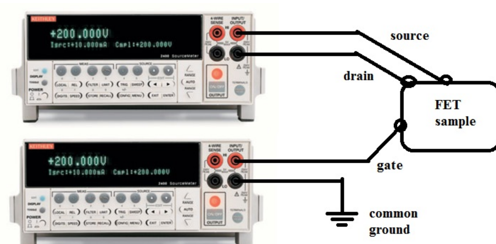

Figure 2.1: Scheme of sample-source meter connection for a FET

A more simple configuration was used for not transfered rubrene sample, bulk or thin film. It need only one source-meter, 6517 electrometer if we need achieve high voltage, or 2614a for IV characterization not above 200V.

Connection between Keithley 2614a and DUT (device under test) is equal to the previous without series resistance. Connection cable is coaxial with BNC connector to reduce external electrical noise. Acquisition system is composed via GPIB conntected with computer through a parallel port (LPT1) or USB. Labview program drives our source-meter.

To perform measurement with rubrene samples in vacuum we used a vacuum chamber. Vacuum is kept by rotative pump of a value about 100$mmTorr$. Also vacuum the chamber has double function, it is projected to perform measure in temperature. the body of chamber

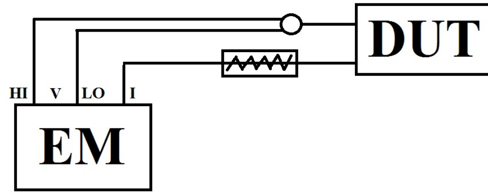

Figure 2.2: Electrometer as source-meter. Series resistance avoids spike current after accidentally breakout of the sample at high voltage

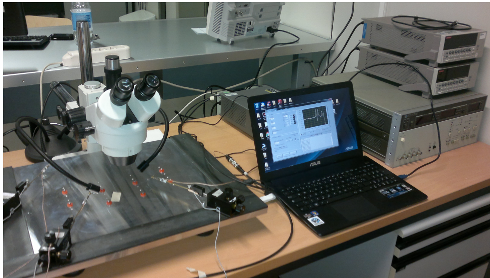

(a)

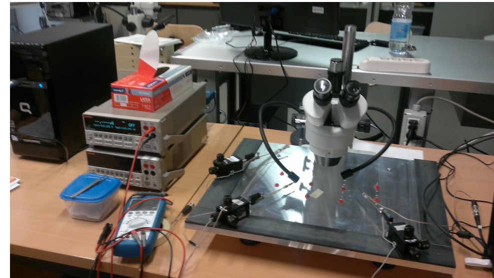

(b)

Figure 2.3: Pictures of current-voltage station in our laboratory

is provided of an internal circuit in which is possible pumps liquid nitrogen or heating sample through joule effect.

(a)

(b)

Figure 2.4: In fig. (a) is reported the vacuum chamber during cooling, note the humidity condensation around tubes to insert liquid nitrogen. In fig (b) the focus is on temperature controller.

To collect electrical current the metallic contact must be deposited on the sample. Deposition of contacts is a crucial step to obtain good quality spectrum, we have to minimize impurities during the deposition and maximize homogeneity of metallic film. Ultra pure gold was choose as contact because of its work function is similar to rubrene work function. To have a gold film of thickness $\sim 100nm$ is necessary of $\sim 150mg$ of gold. As mentioned up the polishing step is really important to avoid the impurities deposition. To clean up gold we immerse gold wire in $Acetone \rightarrow Cloridric\ acid(HCl) \rightarrow distilled\ water\ (H_2O)$ each step

during 5 minutes in ultrasonic bath. After the gold is placed upon a tungsten wire heating by electrical current. Metallic evaporator is kept in high vacuum by a rotative and a turbo-molecular pump. Deposition start when vacuum level is about $10^{-6} Torr$. Channel between two contacts is created using a shadow mask, generally a wire with desired diameter.

2.2 Rubrene Sample

In this thesis work we report analysis operated on different rubrene samples. The differences consist in thickness and structure. All our samples were grown by *Material Science Department of University of Milano Bicocca*, using molecular beam epitaxy (MBE) for thin film and physical vapor transport (PVT) for rubrene bulk. Samples analyzed:

- **Rubrene bulk** (Ru4) upon quartz, with nominal thickness of $10\mu m$
- **AS13104-105a, AS13102-103a, AS106-107a** three samples not transfered with thickness $h = 15, 50, 75nm$ respectively.
- **AS102-103d** not transfered thin film of thickness equal to $h = 50nm$ used to test contact resistance
- **AS1369a** not transfered sample of thickness $h = 30nm$ tested after annealing.
- **AS1306** field effect transistor. Sample transfered on silicon oxide SiO_2 to realize a FET.

(a) AS13104-105a

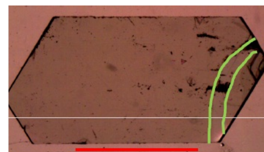

(b) AS13102-103a

(c) AS106-107a

Red line indicates direction of major conduction.

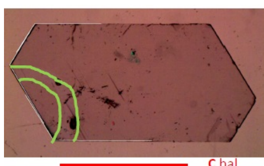

(d)

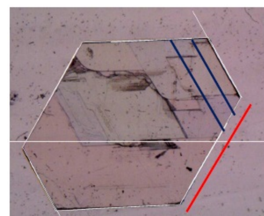

(e)

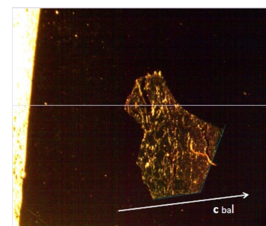

(f)

To improve measurement it's convenient to choose channel in a strong homogeneous region to minimize possibilities to include some crack or visible impurity, we studied our samples with an optical microscopy in transmitted light, dark field and polarized light.

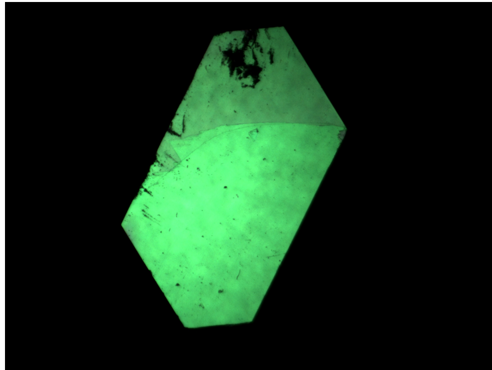

(g) AS13104-105d polarized light

(h) AS13104-105d dark field

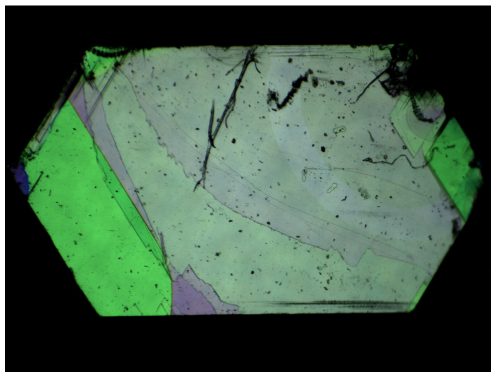

(i) AS13106-107d polarized light

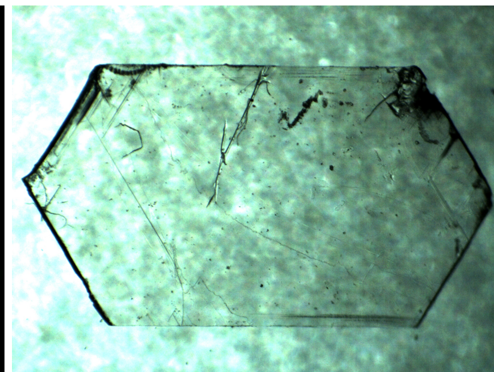

(j) AS13106-107d transmitted light

2.3 Basic Concepts of a Field Effect Transistor

Transistor is the most diffuse device in electronic word. Each of technological object contains millions of transistors BJT, FET, OFET, MOSFET or CMOS. Look that enormously diffusion the research is focused on reduce dimension and improve performances. Organic Field Effect Transistor conjugates a combination of performance, low cost, light weight, and processability. Organic semiconductors are employed as sensors, solar cells, organic didoes and much more. We restrict our area of interest to OFET. The first organic field effect transistor was fabricated in 1982 in which an organic semiconductor replaced silicon. Most of the interest in OFETs system arise from the low thermal budget required to fabricate these devices and their high degree of mechanical flexibility.

Because no covalent bond need to be broken or re-formed, organic semiconductor material can be manipulated using a small energetic input. These weak bonding and ease of manipulation often comes at some price in performances [13]. On the scientific side, OFETs have proven to be a unique tool for investigating charge transport in organic materials. An

OFET is constituted by an **organic semiconductor** $\rightarrow$ **a dielectric layer** $\rightarrow$ **three conducting electrodes**. The device is a sort of pale capacitor where one of the plates is constituted by one electrode, the gate, while the semiconductor element composes the second plate. The other contact, source and drain are directly in contact with semiconductor.

The role of source and drain is to inject and retrieve charge carriers to and from semicon-

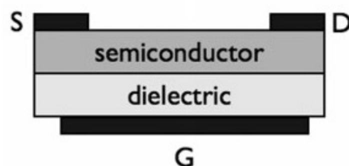

Figure 2.5: One of the most used transistor scheme: bottom-gate, top contacts (BG-TC) [14]

ductor. This electrodes are made principally with gold because most organic transistor are p-channel and then need an high work function contact. Applying a source-gate bias occurs a capacitor charging, the charges are localized at semiconductor-insulator interface, so the distribution of charge carriers in the semiconductor forms a very thin conducting channel.
An organic semiconductor is a quasi-insulator, that is, its density of thermally induced charge carriers is very low (orders of magnitude with respect to inorganic semiconductors). As a consequence, when a voltage V_D is applied between the source and drain, there is no intrinsic conduction but only a flow of charges injected from the electrodes, even if, because of small non-intentional doping, an intrinsic ohmic conduction is always observed when a low voltage is applied to a two terminal single crystal device [15][16]. When V_G become larger then V_T threshold voltage, an equal amount of charge, but opposite in sign, appears at both sides of the dielectric, which results in the formation of the conducting channel. The sign of gate voltage is positive an n-channel and negative for a p-channel. The existence of threshold voltage has various reasons. One of them is the presence of shallow traps in the semiconductor that need to be filled before charges can be inserted in the channel [17]. If the drain voltage is equal to zero, the density of charge is uniform all along the channel. Applying a $V_D > V_G$ a charge is present all along the channel and the drain current I_D grows linearly with V_D. When the drain current increase up to $V_G - V_T$ the potential at a point of the channel close to the drain electrode fall to zero and so does the charge in the channel. This means that the channel is pinched off [14]. At this point the drain current achieve the saturation. A further increase of V_D not increase, significantly, the current.

In this way is possible to obtain the current in a linear region:

$$I_D = \frac{W}{L}\mu C(V_G - V_T - \frac{V_D}{2})V_D, \qquad V_D < V_G - V_T \tag{2.1}$$

Substituting $V_D = V_G - V_T$ is possible to determine the current at the saturation region, the Eq. 2.1 become:

$$I_{Dsat} = \frac{W}{2L}\mu C(V_G - V_T)^2 \tag{2.2}$$

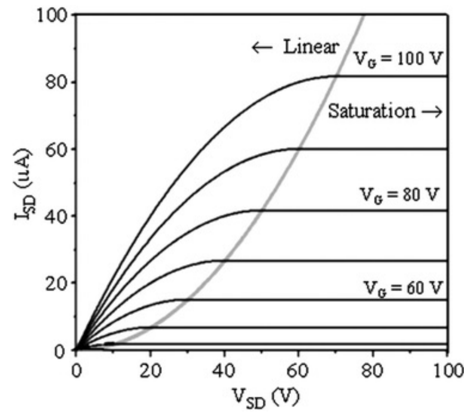

Figure 2.6: Work curves of a standard transistor as reference.

Nowadays there are two parameters of importance to be determined for estimating the quality of an organic transistor: mobility and threshold voltage. Eq. 2.1 e 2.2 are the two most used methods to extract mobility. Rewriting Eq. 2.2 as:

$$\sqrt{I_{Dsat}} = \sqrt{\frac{WC\mu}{2L}}(V_G - V_T) \tag{2.3}$$

Plotting Eq.2.3 vs gate voltage the result will be a straight line. The mobility is obtained from the slope of the line, while the threshold voltage corresponds to the extrapolation of the line to zero current.

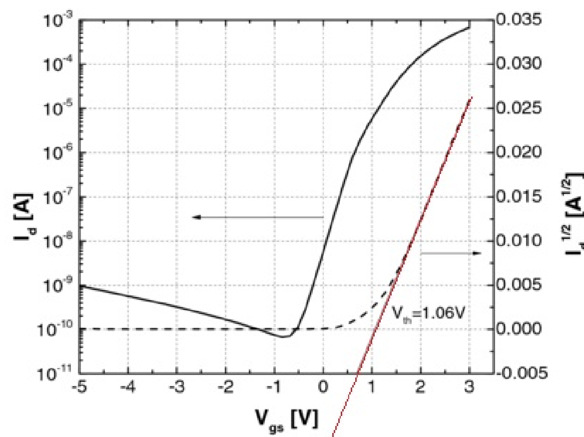

Figure 2.7: An exaple of extrapolation of threshold voltage from transistors curves

2.4 Photocurrent setup

The second setup is the photocurrent system. This is composed by:

- Commercial halogen lamp QTH 24V 150W;
- lens to collimate light beam
- chopper
- monochromator

To collect and analyze data:

- in series with sample we mount a capacitor in parallel with a resistance to acquire signal
- lock-in amplifier
- pc

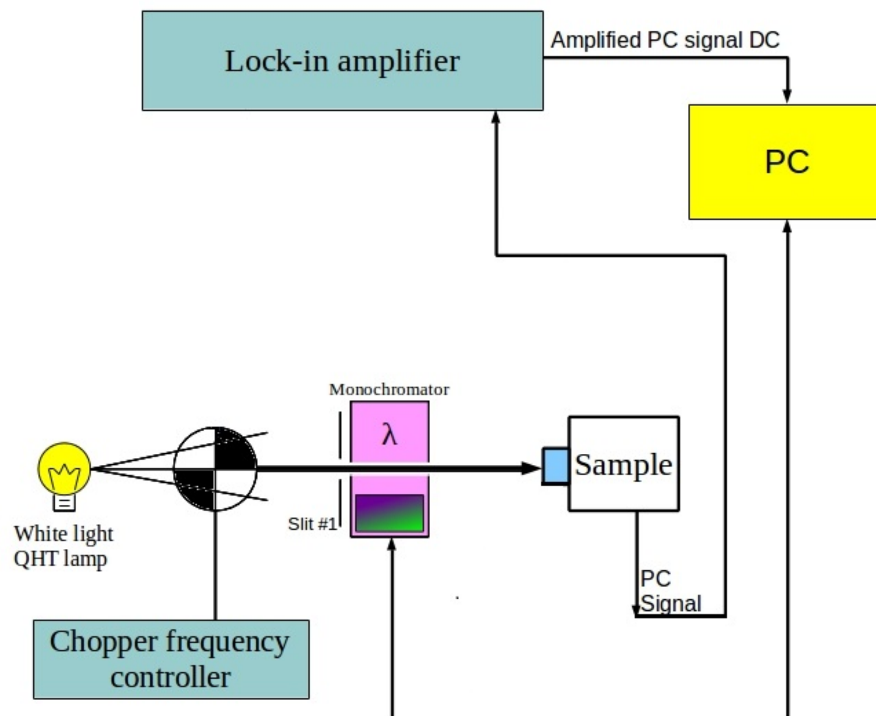

Figure 2.8: Photocurrent apparatus scheme

Samples mounted on a bases with in series capacitance and a resistor in series, as show in fig.2.9.
Value of capacitor is $35nF$, resistance $100K\Omega$. The power supplies applied across samples

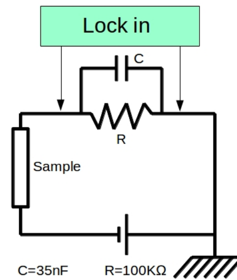

Figure 2.9: Parallel to capacitor and resistance to acquire signal from sample

is necessary to separate exciton (electron-hole pairs) formed by incidence light.

To connect sample and lock-in was used coaxial cable. The lock-in is used to extract signal from noise. It detects signal based on modulation at some known frequency. It is an selective amplifier centered on pass-band filter with well defined frequency ω_0. In our case ω_0 is the frequency of the chopper, tunable by operator. Samples analyzed were the same for IV characteristic: rubrene bulk, three thin film with the three different thickness. Upon on each sample there is two different channel length 50 and 90 μm. In following chapter is reported the detail of rubrene bulk and thin films.
The used slits were 2000, $250\mu m$. We searched the best combination of resistance, bias and slit to collect photocurrent.

Chapter 3

Basic principles of SCLC

3.1 Indroduction

SCLC (space charge limited current) is one of the most used models to analyze organic crystal's properties. SCLC is an easy-to- handle method to obtain several charge-transport parameters like mobility, density of free carriers, density of states and energy distribution of traps., starting by I-V characteristic The earliest theory for SCLC was developed by Mott and Gurney in 1940 [18], and adapted for organic crystal by Mark and Helfrich [cit]. We have three different methods of SCLC with different input and output parameters. In the past decades exponential approach was applied for distribution of trap states, but is necessary to be able to extract the density of traps states without any assumption. The following theory illustrates that an arbitrary shape can be estimate by a current-voltage observations.

3.2 Trap free insulator

SCLC can be divided in three different way: SCLC for a trap free regime, temperature modulated SCLC (TM-SCLC) and differential method (DM-SCLC). The first one is called SCLC trap free insulator. Like input parameters it needs the DOS $h(E)$ to obtain N_t and μ_0. The model consider the parallel-plan capacitor, where the charge density is given by:

$$n = \frac{\varepsilon V}{eL^2}$$

L is the thickness of the insulator (distance between tow contacts), V the applied voltage and ε is dielectric constant. About its value there is a little bit discordance, for example 2.6 in [cit Braga] or 3.5 in [cit Krellner].
There in by applying electromagnetism classical theory following laws result as:

$$j = en(x)\mu_0 E(x) \tag{3.1}$$

Here, we have treated current as a unidimentional problem along x-axes. Differentiating electrical field along the direction of current flow:

$$\frac{dE}{dx} = \frac{en(x)}{\varepsilon} = \frac{j}{\mu_0 E(x)\varepsilon} \tag{3.2}$$

the integration of this differential equation yields the distribution of the electric field inside the sample, the first important expression for SCLC:

$$E(x) = \sqrt{\frac{2j}{\mu_0\varepsilon}} \cdot \sqrt{x} \tag{3.3}$$

Using and it's possible to calculate the distribution of the carrier density:

$$n(x) = \sqrt{\frac{\varepsilon j}{1\mu_0 e^2 \sqrt{x}}} \tag{3.4}$$

Integration of electric field over the sample length gives us the theoretical expression for voltage:

$$V = \int_0^L \sqrt{\frac{2j}{\mu_0\varepsilon}} \cdot \sqrt{x}dx = \frac{2}{3}\sqrt{\frac{2j}{\mu_0\varepsilon}} \cdot \sqrt{L^3} \tag{3.5}$$

This yields Child's law for a perfect trap free insulator:

$$j = \frac{9}{8}\mu_0\varepsilon \cdot \frac{V^2}{L^3} \tag{3.6}$$

.

3.2.1 Geurst law for thin films

The Child's law illustrates in the previous paragraph stands for a 3D geometry. Two basic architectures can be used for a SCLC analysis: sandwich-type geometry (3D), in which both electrodes are on the opposite face of the sample and the the gap structure (2D) where both contacts are deposited in the same side of the sample. The gap structure present two limit case: the thickness h of the film is very small ($h \to 0$), and when the thickness h is higher than the distance between electrodes L. In this seconda case the current is function of h and the equation that describe the IV characteristic is similar to Mott-Gurney equation developed for 3D structure The current for each case is illustrated by:

$$\begin{aligned} I\frac{L^2}{W} &= \frac{2}{\pi}\varepsilon\mu V^2 (film); \\ I\frac{L^2}{W} &= \frac{9}{8}\varepsilon\mu\frac{h}{L}V^2 (bulk). \end{aligned} \tag{3.7}$$

where L is the distances between two electrodes, W the width of channel and h the thickness of sample. μ the mobility, ε the permettivity and V tha applied voltage. Generally, in a thin film at low bias we have an Ohmic behavior, increasing the applied voltage the current that flow into crystal change is trend by transition to a new regime in which $I \propto V^2/L^2$.

For a sample with $h >> 0$ and both electrodes in the same face, we consider an intermediate situation between 2D and 3D structure, the game is payed by h and L ratio. 2D law will dominate as long as $h/L << 1$, while the 3D law will be valid when $h/L >> 1$, or more precisely as long as $(9/8)(h/L) >> (2/\pi)$.
AS deloped by Geurst the current flowing in a thin semiconductor layer between two metallic contact located on the same side of the layer is analyzed using a model in which the thickness of the layer and the electrodes are taken to be negligible compared with the separation of the electrodes. The effect of the traps is taken into account by means of a simple model. If empty traps are present at zero electric field, the theory yields a threshold potential beyond which the current starts flowing. From theory of Mott and Gurney the current should be inversely proportional to the cubic value of channel length. Experimentally Polke, Stuke and Vinaricky found a quadratic inverse proportionality for a thin film. The characteristics were found to be ohmic at low and quadratic at intermediate voltages. The quadratic dependence was attributed to space-charge limited currents, but difficulties arise in the quantitative interpretation.

3.3 Correction to perfect trap free insulator

In real case organic crystals are not perfect and trap levels play a not negligible role, then Child's law need correction to be applied.
In order to catch out information about current-voltage traps, a parameter θ defined by ratio of free to total carrier concentration must be considered during the law's formulations: $\theta = n_f/n$. Because traps diminishing current across sample Child's current became:

$$j = \frac{9}{8}\theta\mu_0\varepsilon\frac{V^2}{L^3} \tag{3.8}$$

Factor θ depends on traps distribution, they can be gaussian, linear or parabolic form as indicated in a following table [cit.krellner]: In the table table1 it is possible to see that E_t a discrete trap level affect on sclc curve only if it lies below E_F Fermi level. In this case the trap level is called *shallow*, otherwise E_t is a deep trap.
Trap levels play a very important role on the conduction process. In fact, whenever carriers come injected in, Fermi's level pulls up toward conduction band. Doing so, carriers would remain trapped therefore, unable to contribute to the current flow.. If $E_F = E_t$ the current shows a quasi vertical increase, the trap is filled up and carriers injected can reach conducting band, the result is current predicted by Child's law. In the previous scheme we assumed a temperature equal to zero: $T = 0K$. The curve is divided in four zones:

Distribution	Mathematical expression	$j(U)$	$m = \frac{\partial \log j}{\partial \log U}$
Discrete trap level	$N_t\delta(E - E_t)$	$\frac{9}{8}\mu_0\epsilon\frac{N_b}{N_t}\frac{U^2}{L^3}\exp -(\frac{E_t}{k_BT})$	$m = 2$
Exponential trap distribution	$\frac{N_t}{E_t} \times$ $\exp(-\frac{(E-E_c)}{E_t})$	$e^{1-l}\mu_0\epsilon^l\frac{N_b}{N_t}(\frac{l}{l+1})^l(\frac{2l+1}{l+1})^{l+1}\frac{U^{l+1}}{L^{2l+1}}$	$m = 1 + l$ $l = \frac{T_t}{T}$
Gaussian trap distribution	$\frac{N_t}{\sqrt{2\pi\sigma^2}} \times$ $\exp(-\frac{(E-E_t)^2}{2\sigma^2})$	$e\mu_0\epsilon\frac{N_b}{N_t}\exp(-\frac{E_t+\sigma^2/2k_BT}{k_BT})$	$m = 2$ $E_F > E_t + \frac{\sigma^2}{k_BT}$
		$e\mu_0N_b\exp(-\frac{E_t}{k_BT} + 2)\frac{U}{L}\times$ $\exp\left[-\sqrt{[\frac{2\sigma^2}{(k_BT)^2} + 8](\frac{eL^2N_t^*}{\epsilon U})}\right]$	$m > 2$ to ≈ 4 $E_F > E_t$
		$\frac{e\mu_0U}{L}\frac{(\epsilon U)^\alpha N_b}{(eL^2N_t-\epsilon U)^\alpha}\exp(-\frac{E_t}{k_BT})$ with $\alpha = \sqrt{1 + \frac{\pi}{8}(\frac{\sigma}{k_BT})^2}$	$m > 3$ to ≈ 8 $E_F < E_t$

Table 3.1: Current-voltage relations for typical trap distributions. N_t is the total trap density, Nb is the density of the extended states, and Et is the energetic position in the gap. For the exponential distribution is Et = kBTt. [19]

-a Ohmic region. Here carriers are thermally generated.
-b shallow traps dominate. -c traps are filled by injected carriers. -d trap free regime.
In a real case of finite temperature vertical region is smoothing by thermodynamic statistic of Fermi function.

For most experimental SCLC curves m value is not a constant over entire voltage range. Therefore $m = 2$ is not a sufficient parameter to identify the trap filled limit, but is a reliable indicator.

The error is evidenced by the formulation of effective mobility which depends on second power of voltage:

$$\mu_{eff} = \mu_0\theta = \frac{8jL^3}{9\varepsilon V^2}\theta \tag{3.9}$$

Value of μ_{eff} is lower than μ_0 because $\theta < 1$. In a I-V characteristic we recognize a trap fill limit due to a change of m, from a value above 2 to value equal 2. The voltage value which

separates two regimes is called V_{TFL}. This is the one of most important value obtained experimentally. From this we can calculate the total traps density from relation:

$$N_t = \frac{\varepsilon V_{TFL}}{eL^2} \tag{3.10}$$

This theory is used for Rubere's sample at room temperature and atmospheric pressure. In the experimental section it may be discussed on details the procedure adopted to characterize our sample a the results obtain to calculate DOS, N_t total trap density and above all μ the mobility.

3.4 Differential Method of SCLC

This method looks simple and it allows to calculate the $h(E)$ but, it show limits. Nespurek and Sworakowki in [20] have given a cartian value of Fermi level in contrast with Arkhipov et al [21] however we explain briefly the DM-SCLC. Starting by [20] Differential method is valid under the following assumption:

- it's considered a plane parallel sample of a uniform dielectric. The density of traps and mobility is assumed constant over sample. Two contacts are placed at $x = 0$ and $x = D$.
- Like reference on Energy scale we choose the band edge with positive direction towards the band (valid for both electrons and holes).
- the diffusion current carries is neglected.
- To describe the free carriers density we use Boltzmann statistics and Fermi-Dirac statistics for trapped carriers:

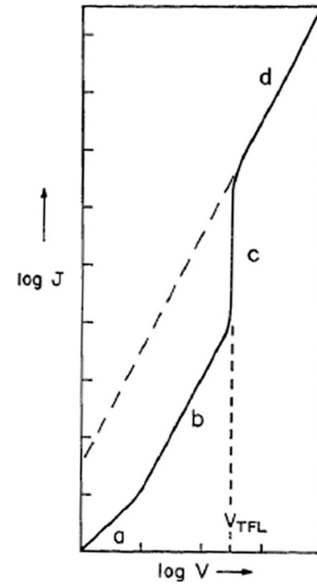

Figure 3.1: Schematic voltage dependence of the SCL current in an insulator with one descrete shallow trap level (W.Helfric)

Starting point is the definition of electrical field and related Fermi's energy:

$$F(D) = \kappa_1 \frac{V}{D} \tag{3.11}$$

where $1 \leq \kappa_1 \geq 2$. And quasi-Fermi level at the counter electrode is determined from eq:

$$E_f(D) = kTln\frac{D}{\kappa 1 N_0 e\mu} + kTln\frac{j}{V}. \tag{3.12}$$

A shift of the quasi Fermi level on changing the voltage applied to the sample causes the occupancy of traps to change, and in consequence enables one to scan the energetic distribution at the collecting electrode.
To obtain information we differentiating the total to free carrier ratio (θ^{-1}) with respect to $E_f(D)$, after several manipulations one obtains:

$$\frac{dn_t}{(n_f+n_t)d(E_f/kT)} = \frac{1}{m-1} - \theta \tag{3.13}$$

If $\theta \leq 1$ eq 3.13 became:

$$\frac{dlnn_t}{d(E_f/kT)} = \frac{1}{m-1} \tag{3.14}$$

, where m is the slope of the current-voltage curve in the bilog system $(m = dlnj/dlnV)$. Continuing to assume (θ^{-1}), and approximate $n_t \approx N_t$ and $h(E) \approx n_t(E)$ we can obtain:

$$h(E_f) = \frac{n_0}{kT(m-1)} exp\left(\frac{1}{kT}\int_{E_0} E_f \frac{1}{m-1} dE_f\right) \tag{3.15}$$

$n_0$andE_0 are boundary values of $n_t$andE_f. Using 3.12, 3.15 become:

$$h(E_f) = \frac{A}{kT}\frac{V}{m-1} \tag{3.16}$$

where $A = n_0/V_0$, V_0 is lowest voltage applied to the sample during an experimental run.
If the sample reaches the trap free limit (injected carries fill the whole traps level and m=2 at this voltage) we are able to extract density of state as:

$$N_t = n_0\left(\frac{2V_{TFL} - V_0}{V_0}\right)h(E_f) = \frac{\varepsilon\kappa_1\kappa_2}{2eD^2kT}\frac{V}{m-1} \tag{3.17}$$

The constant parameters $\kappa_1$andκ_2 describe the spatial distribution of the electric field through the sample, which can be rewritten in the more precise theory presented by [22] as:

$$\kappa_1 = \frac{(2m-1)}{m}\text{and}\kappa_2 = \frac{(m-1)}{m}(1+C) \tag{3.18}$$

However about [20] $1 \leq \kappa_1 \leq 2$and$\frac{1}{2} \leq \kappa_2 \leq 1$. We derived the set of previous equation from an arbitrary distribution of traps from a single experimental current-voltage characteristic. In this method the problem of the correct determination of the energy axis for the extracted density of trap states still left open.

3.5 Temperature modulated SCLC

After the development of DM-SCLC some inaccuracies remain, which are due to the local distribution of the electric field trough the sample. Another problem consists in boundary conditions of the energy integral discussed in par. 3.4. To improve that theory Schauer

worked on a new model called TM-SCLC [23]. It is possible to show that last method give reliable results on the values of DOS distributions, without any sharp distributions consideration and assumption.
To apply TM-SCLC we assume: [22]:

- AS in DM-SCLC we consider a plane parallel sample and it assumed that the mobility of the charge carriers and the trap density is constant throughout the sample.
- Carriers of one sign (holes) are injected from an ohmic contact placed at $x = 0$.
- L (electrical length) is independent of the applied voltage.
- Diffusion of carriers is not considered
- Quasi-equilibrium is reached at any injection level
- The energetic scale is choose to have zero point ant the band edge and growth toward energy gap

Starting point is always Ohm's law:

$$j = e\mu_0 n_f(x)F(x) \tag{3.19}$$

and the Poisson equation:

$$\frac{dF}{dx} = -\frac{en_s(x)}{\varepsilon} \tag{3.20}$$

Symbols have the same previous meaning, just a notification about $\varepsilon = \varepsilon_r\varepsilon_0$ is the product of permittivity and the dielectric constant (permittivity is a value included $2.6 \leq \varepsilon_r \leq 3.5$).
The first derivative of Eq.3.19 yields:

$$\frac{dF}{dx} = -\frac{j}{e\mu_0 n_f^2}\frac{dn_f}{dx} \tag{3.21}$$

Putting 3.21 into Eq.3.20:

$$\frac{dn_f}{dx} = \frac{e^2\mu_0}{j\varepsilon} n_f^2 n_s \tag{3.22}$$

and integrating along the sample direction x:

$$\int_{n_{f0}}^{n_{fL}} \frac{dn_f}{n_f^2 n_s} = \int_0^L \frac{e^2\mu_0}{\varepsilon j} dx \tag{3.23}$$

Finally we obtain an inversion current density Y:

$$Y \equiv \frac{1}{j} = \frac{\varepsilon}{e^2\mu_0 L}\int_{n_{f0}}^{n_{fL}} \frac{dn_f}{n_f^2 n_s} \tag{3.24}$$

Here n_{fL} meaning $n_f(x = L)$ and similarly $n_{f0} = n_f(x = 0)$ for the free carrier concentration at the cathode of the sample.

For an Ohmic contact is not wrong to approximate injected carriers as infinite number: $n_{f0} = \infty$ which means tha electric field at $x = 0$ drops to zero. Now combining the expression of electric field: $F = dU/dx$ with Ohm's law Eq.3.19 and Eq.3.22

$$-dV = Fdx = \frac{j}{e\mu_0 n_f(x)}dx = \big(\frac{j}{e\mu_0}\big)^2 \frac{\varepsilon}{e} \frac{dn_f}{e[n_f(x)]^3 n_s} \tag{3.25}$$

Integrating again gives:

$$Z \equiv \frac{V}{j^2} = \frac{\varepsilon}{e^3\mu_0^2} \int_{n_{f0}}^{n_{fL}} \frac{dn_f}{n_f^3 n_s} \tag{3.26}$$

To take an more useful form differentate Z with respect to Y as final result:

$$\frac{dZ}{dY} = \frac{\varepsilon e^2 \mu_0 L}{e^3 \mu_0 \varepsilon} \frac{dn_f}{n_f^3 n_s} \frac{n_f^2 n_s}{dn_f} = \frac{L}{e\mu_0 n_f} \tag{3.27}$$

This derivative can also be expressed as function of m, the slope of double-logarithmic current-voltage characteristic

$$m = \frac{d\ln j}{d\ln V} \tag{3.28}$$

Rewriting Eq.3.27 in terms of $\partial j/\partial V = mj/V$ we gain the first equation that describes the current-voltge relation of SCLC:

$$\frac{V}{j}\frac{(2m-1)}{m} = \frac{L}{e\mu_0 n_f} \tag{3.29}$$

The same procedure can be applied to obtain the second derivate of Z with respect to Y:

$$\frac{d^2Z}{dY^2} = \frac{d}{dY}\left(\frac{L}{e\mu_0 n_f}\right) = \frac{eL^2 n_s}{\varepsilon} \frac{d\frac{n_f^2}{n_f}}{dn_f} = \frac{n_s e L^2}{\varepsilon} \tag{3.30}$$

and

$$\begin{aligned} \frac{d^2Z}{dY^2} = \frac{d}{dY}\left(\frac{V}{j}\frac{(2m-1)}{m}\right) &= \frac{(2m-1)}{m}\frac{1}{j}\frac{\partial V}{\partial(\frac{1}{j})} + V\frac{(2m-1)}{m}\frac{\partial(\frac{1}{j})}{\partial(\frac{1}{j})} + \frac{V}{j}\frac{\partial(2-\frac{1}{m})}{\partial(\frac{1}{j})} \\ &= -\frac{V}{m}\frac{(2m-1)}{m} + V\frac{(2m-1)}{m} - \frac{V}{m^3}\frac{\partial m}{\partial lnV} \end{aligned} \tag{3.31}$$

Combining Eq.3.30 and Eq.3.31 gives the second general equation of the current-voltage characteristics of SCLC:

$$\left[\frac{(2m-1)}{m}\frac{(m-1)}{m}(1+B)\right]V = \frac{n_s e L^2}{\varepsilon}. \tag{3.32}$$

B is an abbreviation which reflects the influence of the second derivative of current on the total charge carrier concentration n_s

$$B = \frac{-1}{m(m-1)(2m-1))}\frac{\partial m}{\partial lnV} \tag{3.33}$$

Defining σ_{SCL} as electrical conducivity under SCLC conditions and the generalized Ohm's law became:

$$j = \sigma_{SCL} F = e\mu_0 n_f \frac{V}{L}\frac{(2m-1)}{m} \tag{3.34}$$

Term $(2m-1)/m$ represent the nonhomogeneity of the electric field in the sample. From eq. 3.29 and Eq.3.32 we can extract the correction to trap free insulator case, $\theta = n_f/n_s$ as the crucial parameter:

$$\theta = \frac{n_f}{n_s} = \frac{m^3 jL^3}{(2m-1)^2(m-1)(1+B)\varepsilon\mu_0 V^2} \tag{3.35}$$

Knowing *theta* it's possible to take out another important transport parameter, the effective mobility $\mu_{eff} = \theta\mu_0$. The effective mobility is crucial parameter because can be extract directly from experimental data without any additional assumptions about the shape of density of trap stats:

$$\mu_{eff} = \frac{j}{\varepsilon}\frac{L^3}{V^2}\frac{m^3}{(2m-1)^2(m-1)(1+B)} \tag{3.36}$$

3.6 The density of States (DOS)

n_s the total charge density is determined by Fermi-Dirac statistics

$$n_s = \int dEh(E)f(E,E_F,T) \tag{3.37}$$

where

$$f(E) = \frac{1}{1+exp(\frac{E-E_F}{k_B T})} \tag{3.38}$$

and $h(E)$ is the density of states (DOS). The determination of the DOS function is based on the concept of finding an expression for the increment of the space charge as the position Fermi level changes.
Deriving Eq. 3.41 with respect to Fermi energy:

$$\frac{dn_s}{dE_F} = \int h(E)\frac{df(E,E_F,T)}{dE_F}dE = \int \frac{h(E)}{k_B T} f(1-f)dE \tag{3.39}$$

In other words is possible describe the increment of space charge density using the logarithm of the free carrier density,

$$\frac{dn_s}{dE_F} = -\frac{1}{k_B T}\frac{dn_s}{dlnn_f} \tag{3.40}$$

Taking in a count Eq to write space charge density

$$n_s = \frac{\varepsilon V}{eL^2}\left[\frac{(2m-1)}{m}\frac{(m-1)}{m}(1+B)\right] \tag{3.41}$$

with

$$n_f = \frac{Lj}{e\mu_0 V}\frac{m}{(2m-1)} \tag{3.42}$$

Because of Eq. 3.41 we can express Eq. 3.39 in following way:

$$\frac{dn_s}{dE_F} = -\frac{1}{k_B T}\frac{\varepsilon}{eL^2}\frac{d[V(2m-1)(m-1)(1+B)/m^2]}{dlnn_f} \tag{3.43}$$

C factor is taken by Schauer et al. [23]. So in a more compact expression

$$\frac{dn_s}{dE_F} = \frac{1}{k_B T}\frac{\varepsilon V}{eL^2}\frac{(2m-1)}{m^2}(1+C) \tag{3.44}$$

where

$$C = \frac{B(2m-1)+B^2(3m-2))+\frac{d[ln(1+B)])}{dlnV}}{1+B(m-1)} \tag{3.45}$$

Density of states is still unknown but to obtain its value is necessary to deconvolve Eq.3.44 with respect to df/dE_f. As suggest by [22] cubic spline approximation is a good enough method, in which the experimental data are fitted using cubic spline and changes each of the four coefficients on the moment of the deconvolution function. Trough these calculated coefficient DOS $h(E)$ can be reconstructed. Cubic spline method work better in a low temperatures regime $(100K-200K)$ because the derivative of Fermi-Dirac function is a sharp peak around the Fermi level , minimizing the associated error.

3.7 Cubic spline deconvolution method

This method was developed by Deutsch et al. using spline functions. Experimentally Dn_s/dE_F is available. More generally a convolution is defined with:

$$J(t) = \int_{-\infty}^{\infty} K(s)J_0(t-s)ds \tag{3.46}$$

In our case $J_0(t)$ is represented by $h(E)$ instead $K(s)$ is the derivative of Fermi-Dirac distribution function.

Cubic spline is defined by sum of function:

$$J(t) = \sum_k s_k(t) \tag{3.47}$$

where $s_k(t)$ is a polynomial for each interval:

$$s_k(t) = \begin{cases} 0, t < \chi_k \\ A_k t^2 + B_k t^2 + C_k t + D_k, \chi_k < t < \chi_{k+1} \\ 0, t < \chi_{k+1} \end{cases} \tag{3.48}$$

As illustrated in the next operations is resumed in following steps:

- fit a stepwise cubic spline to the $J(t)$ data. This determines the coefficients $A_k, B_k, C_k D_k$ for the measured $dn_/dE_F(E_F)$

- Caluculate the first four moment M of the resolution function $K(s)$.

$$M_\alpha = \int_{infty}^{\infty} s^\alpha K(s) ds \qquad (3.49)$$

in our case we have $M_0 = 1$, $M_1 = 0$, $M_2 = \pi^2/3(k_BT)^2$ and $M_3 = 0$.

- At least we have to compute coefficients a_k, b_b, c_k, d_k as:
$a_k = A_k/M_0 = A_k$
$b_k = B_k/M_0 + 3a_kM_1/M_0 = B_k$
$c_k = C_k/M_0 + 2b_kM_1/M_0 - 3a_kM_2/M_0 = C_k - (\pi k_BT)^2 A_k$
$d_k = D_k/M_0 + c_kM_1/M_0 - b_kM_2/M_0 + a_kM_3/M_0 = D_k - (\pi k_BT)^2 B_k$

In this way is possible to completely determine the $h(E)$ function if the intervals χ_k pf the cubic spline is the same.

3.8 Relevant Energy Levels

An addition experimental input is necessary. Activation energy E_A is the distance between Fermi level and the nearest transport band. This energy would be dependent from temperature. Such definition of activation energy is true is E_F is independent from temperature, but it's not so obvious. Assuming that transport is due to holes (positive carriers) the band edge is situated at E_V. If we approximate the E_F temperature independent then is possible to write activation energy in the following way:

$$E_A = -\frac{ln\sigma}{d(1/k_BT)} = E_{F0} - E_V = E_F(T) + \gamma_F k_BT - E_V \qquad (3.50)$$

where $E_F(T)$ is substituted with his the Taylor's series around $T = 0K$. The factor γ_F is the statistical shift of Fermi level, different for hole and electron transport. Here we can define electrical conductivity as:

$$\sigma = \sigma_M \big(-\frac{E_F(T) - E_V}{k_BT} \qquad (3.51)$$
$$\sigma_M = e\mu_0 N_b \text{is the microscopic conductivity}$$

In SCL transport model and with activation energy concept we are able to redefine the conductivity as:

$$\sigma_{SCL} = \frac{jL}{V} = \sigma_M \big(\frac{2m-1}{m}\big) exp\big(-\frac{E_F(T) - E_V}{k_BT}\big) \qquad (3.52)$$

In the same way the redefinition of activation energy is:

$$E_A^{SCL} = -\frac{dln\sigma - SCL}{d\frac{1}{k_BT}} = -\frac{dlnj}{d\frac{1}{k_BT}} \qquad (3.53)$$

The aim of this work is to find the energy level where the additional amount of injected space charge described by dN_s/DE_F is centered. The starting point is the derivative of Fermi level with respect to temperature. Using only the carrier conservation, it takes the form:

$$\frac{dE_F}{dT} = \frac{1}{T}\frac{\int h(E)(E_F(T)-E)f(E,E_F,T)[1-f(E,E_F,T)]dE}{\int h(E)f(E,E_F,T)[1-f(E,E_F,T)]dE} \tag{3.54}$$

We will use Eq.3.54 to reconstruct the correct DOS. Also this equation represent the shift of Fermi level with respect to the temperature. Modifying left side of previous equation with linear form of Fermi level and combining it with Eq. 3.51 we obtain the final expression for the activation energy and the correlated energy dominating the injection of space charge in SCLC measurements E_D:

$$\mathbf{E_D = E_A^{SCLC} + \frac{(3-4m)n}{(2m-1)(m-1)m}kT + \frac{dln(1+B)}{dln(1/kT)}} \tag{3.55}$$

The dominating energy together with Eq.3.44 gives the complete reconstruction of the trap density of states from temperature dependent SCLC measurements.

3.9 Space-Charge-limited currents in organic films: Some open problems

Among the of factor that affects on the IV characteristics there are temperature, presence of carrier traps and their distribution in energy, spatially inhomogeneity of the sample and electrode configuration [24]. Of course SCLC theory previously illustrated takes in account this effects and use them to extract physical and structural informations from IV curves, but as other model, it presents some limitations and its employment leads various errors.
That usually occur examples of errors which occur are: influence of spatial trap distribution on the shape of current-voltage characteristics, current noise, polaron formation, etc. During the solutions of SCL current-voltage characteristic it can be assumed that the injection level to be sufficiently high, therefore, the concentration of thermally generated carriers will be negligibly small compared with that of injected ones, i.e. $n_{s0} = 0$. Also we shall neglect the contribution of the diffusion current and consider that the sample being spatially uniform, i.e., $N_t \neq N_t(x)$ and symmetric, we shall use the same equation for both, electron and hole currents. When the sample presents inner traps we must introduce the free-total-carrier concentration ratio θ. At this point we take in account that the SCL current-voltage characteristic depends on the position of the quasi-Fermi level at the collecting electrode, $E_F(L)$, with respect to energies of the distribution of local states. Generally the parameter θ is function of position x, or better: $\theta = \theta(x)$, but with this assumption the dependence restricted only at L value: $\theta(L)$. from this assumption we obtain the 3.8. Another possible error is done about DM-SCLC putting $C = 0$ method makes an error about 2% in DOS and neglecting B factor the error is about 10%. In both case quasi Fermi level is not influenced by the simplification. A substantial error may be introduced by setting constant the first order factors κ_1 and κ_2

Eq.3.18. As mentioned above the value of that factors are: $1 < \kappa_1 < 2$ and $\frac{1}{2} < \kappa_2 < 1$, but assuming $\kappa_1 = \kappa_2 = 1$, one introduces at most 100% error in the DOS function and a ca kT shift in the position of the quasi-Fermi level.
surface electrode configuration almost all expressions concerning SCLC theory presented in literature have been derived for the bulk structures, where the electrical contacts are placed in a top-bottom configuration. But in our sample we preferred the co-planar structure (gap). Guerst first derived a simplified equation for surface SCLC, latter on the equation was modified with more precision for three different electrode configuration. An attempt to find a general equation for SCL current independent by electrode configuration using E-infinity theory [**?**] has been made by Zmeskal et al. [25] Ad shown in figure below, only one electrode works as injecting contact and the current in a sample with monoenergetic traps ($h(E) = N_t\delta(E - E_t)$) current becomes:

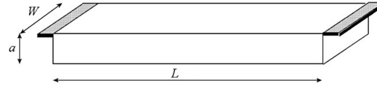

Figure 3.2: Sample geometry of gap structure

$$I \simeq \mu\varepsilon\varepsilon_0\theta\frac{V^2}{L^2}arctan(\frac{2a}{L})W \tag{3.56}$$

where the parameters are illustrate in fig. The expression is similar to this for sandwich sample: it predict identical voltage dependences, differing in thickness dependences. However, for $y = (2aW/L) \leftarrow 0$, $arctan(y) \simeq y$, hence for sufficiently thin sample Eq fir current become identical with Eq.(3.8), to within an insignificant factor of order unity.

Chapter 4

Experimental Results

4.1 Introduction

In this chapter is reported electrical characterization of rubrene crystals with different thickness: thick bulk crystals and very thin highly oriented films.
Samples are grown by Material Science Department of University of Milano Bicocca.
The aim of current-voltage (I-V) analysis consist in calculation and extrapolation of electrical parameters like mobility, traps density or density of states. These are important quantities to determine quality of rubrene and its possible application for electronic device. Mott-Gurney and Geurst models are employed to obtain mobility and trap density, for bulk and thin film respectively. SCLC occurs for density of state (DOS) and transmission line model for contact resistance. The current-voltage characteristic was measured by applying a voltage with a source meter Keithley 2612a or 6517 electrometer described in Chapter 3.

Sample	Substrate	Thickness	Experiment
Ru4	quartz	$10\mu m$	IV, PC
AS13104-105a	none	$15nm$	IV, PC
AS13102-103a	none	$50nm$	IV, PC
AS13106-107a	none	$75nm$	IV, PC
AS1306-07b	SiO_2	$45nm$	IV, TFT
AS1369a	none	$30nm$	IVT
AS13102-103d	none	$50nm$	IVT, TLM

4.2 Rubrene bulk

Crystal of rubrene bulk (Ru4) grown with PVT technique on quartz substrate.
Electrical characterization was performed on air and room temperature. Metallic gold contacts were deposited by thermal evaporation, heating a tungsten wire in the HV(high vacuum: $10^{-6} Torr$) chamber.

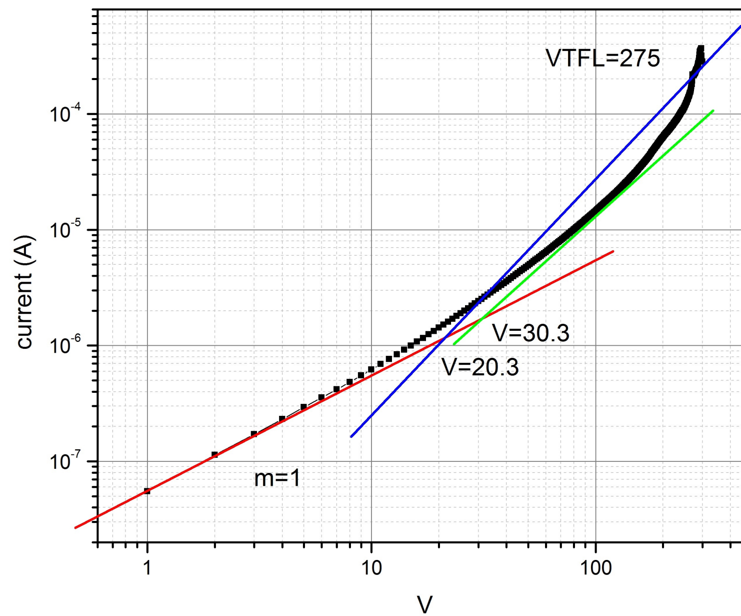

(a)

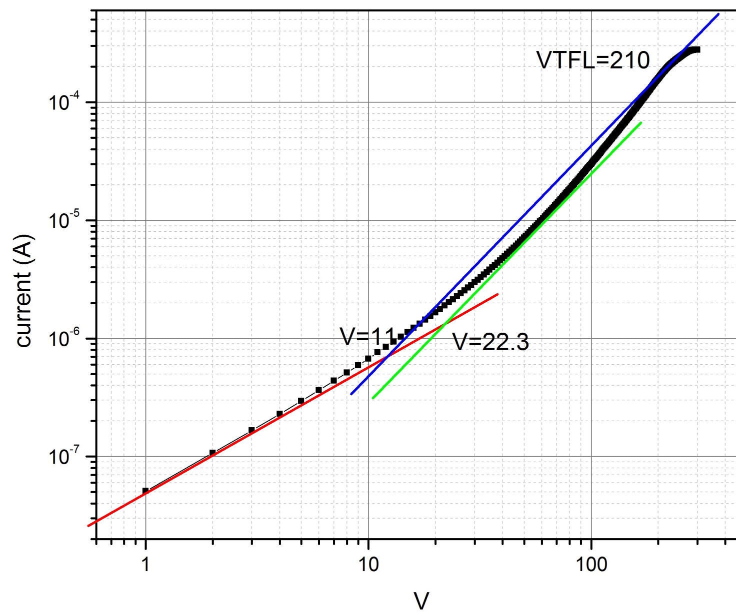

(b)

Figure 4.1: Crystal of Rubrene bulk. IV charcacteristic in dark (a) and light (b)

IV spectrum were collected in three steps:

- first run from 0 to 700 bias and keeping dark room
- second run from 0 to -700V to discharge sample
- third run from 0 to 700 V illuminated sample

The results presented in tab.4.1 are consistent with literature for samples with similar characteristic. In next table our own values compared with **??**. Physical dimensions of our sample are: indicative thickness $h = 10\mu m$ and contact width $W = 0.5cm$, channel length $L = 50\mu m$.

	[16]	Dark	Light
$V_{TFL}(V)$	130	275	210
$I(A)$	$6.3 \cdot 10^{-4}$	$2.17 \cdot 10^{-4}$	$1.8 \cdot 10^{-4}$
$\mu(cm^2/V)s$	3.5	2.06	2.87
θ	0.2	0.66	0.5
$N_t(cm^{-3})$	$5.2 \cdot 10^{13}$	$1.47 \cdot 10^{13}$	$1.12 \cdot 10^{13}$

Table 4.1: Rubrene single crystal bulk electrical parameter

4.3 Rubrene thin films

After rubrene bulk we have tested three rubrene thin films with different thickness: $AS13104 - 105a$, $AS13102 - 103a$ and $AS13106 - 107a$ with $h = 15, 50, 75nm$ respectively. In Fig. 4.2 the red line indicates ohmic region, green line SCLC with traps and blue line stands for trap free region. On the graph is written values for V_Ω, $V_{\Omega'}$ and V_{TFL}. V_Ω and $V_{\Omega'}$ are useful to calculate θ the ratio between the density of free carriers achieved under injection and the total density of injected carriers, trapped and free. We can express θ in terms of voltage because the presence of shallow trapping delays the finish of the Ohmic regime from the critical voltage V_Ω to $V_{\Omega'} = (1/\theta)V_\Omega$ [**?**].

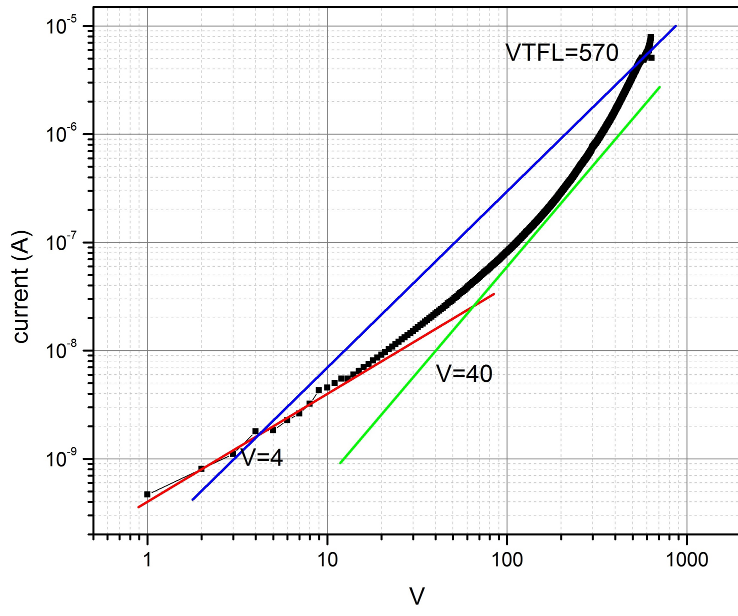

(a)

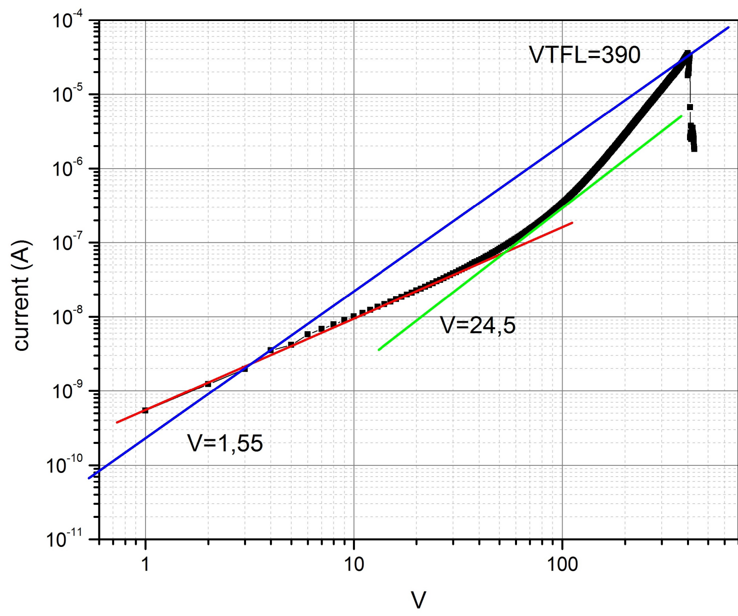

(b)

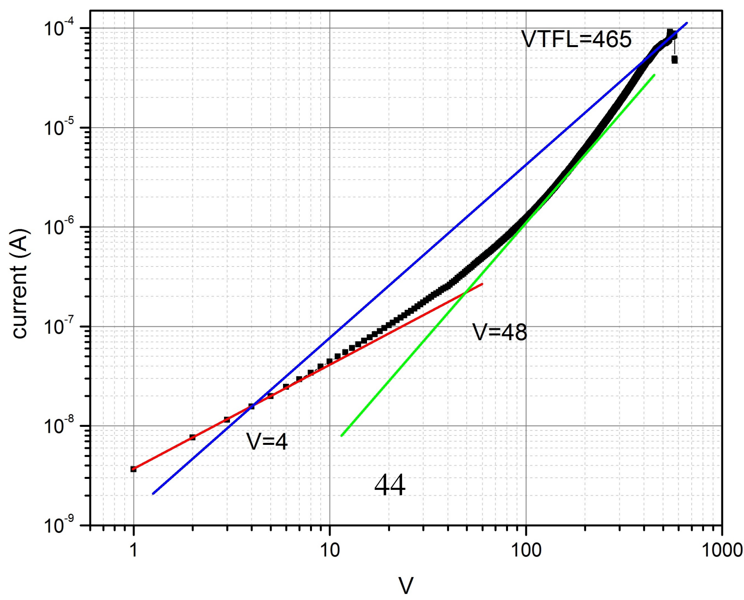

(c)

In the following graphs we compare behavior of different thickness with different channel length.

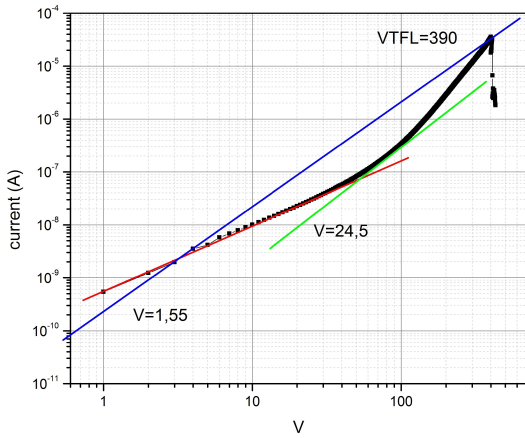

(a) $h = 50nm$, channel lenght $L = 60\mu m$

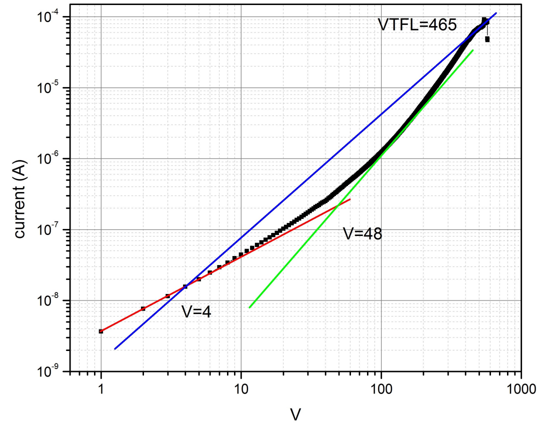

(b) $h = 75nm$ and $L = 60\mu m$

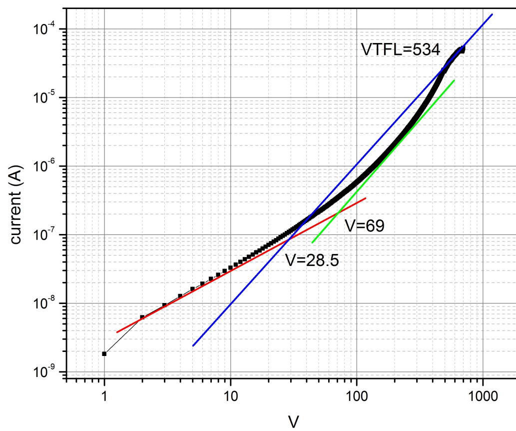

(c) $h = 50nm$ and $L = 90\mu m$

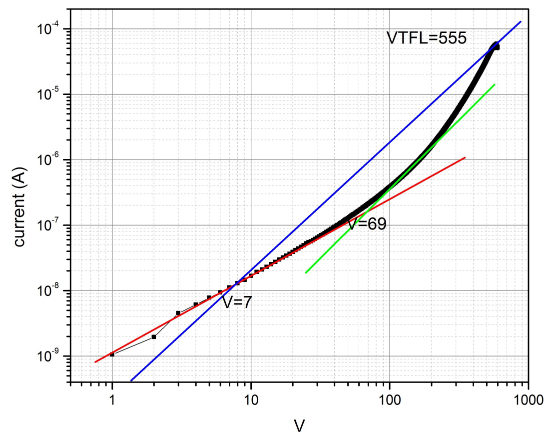

(d) $h = 75nm$ and $L = 90\mu m$

In this case contact width is about $W \simeq 0.3cm$. We can see that increasing channel length increase V_{TFL} too.

	AS13104-105a	AS13102-103a		AS13106-107a	
$h(nm)$	15	50		75	
$L(\mu m)$	60	60	90	60	90
$V_{TFL}(V)$	570	390	534	465	555
$I(A)$	$5.1 \cdot 10^{-6}$	$3.1 \cdot 10^{-5}$	$3.1 \cdot 10^{-5}$	$6.1 \cdot 10^{-5}$	$5.1 \cdot 10^{-5}$
$\mu(cm^2/Vs)$	$9.5 \cdot 10^{-3}$	0.12	0.15	0.17	0.22
θ	0.05	$6.3 \cdot 10^{-2}$	0.4	$8.5 \cdot 10^{-2}$	0.1
$N_t(cm^{-3})$	$3.06 \cdot 10^{13}$	$5.3 \cdot 10^{13}$	$1.2 \cdot 10^{13}$	$2.5 \cdot 10^{13}$	$1.3 \cdot 10^{13}$

Table 4.2: Electrical parameters. Samples with different characteristics of thickness and channel length

From Tab.4.2 the mobility increases with thickness and V_{TFL} depends on channel length as explained by Geurst in **??**

To avoid wrong interpretation of IV curves due to a possible sample breakdown followed by the complete trap-free-regime, we have analyzed the characteristic trough differential SCLC method (DM-SCLC). Theory of DM-SCLC is illustrated in Chapter 4.

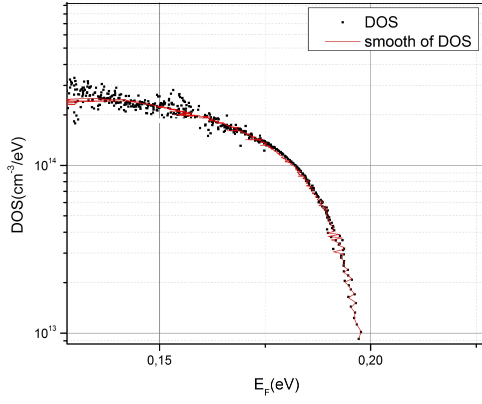

(e) DOS vs Ef $h = 15nm$ and $L = 60\mu m$

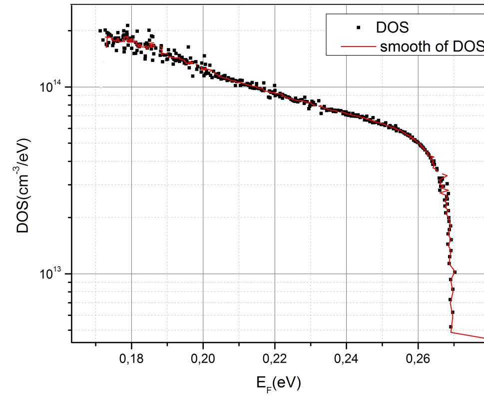

(f) DOS vs Ef $h = 50nm$ and $L = 60\mu m$

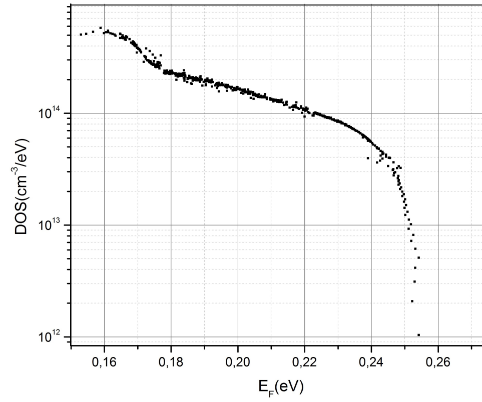

Figure 4.3: DOS vs Ef $h = 75nm$ and $L = 60\mu m$

This method is based on assumption that changing the position of quasi Fermi level E_F (increasing applied bias), is possible determine trap distribution for which the occupancy is changed. Assuming the zero-temperature statistic, it is possible to estimate the parameters of an arbitrary distribution of traps, knowing the function describing the distribution $h(E_F)$ Eq.3.15 and the position of the quasi-Fermi Eq.3.12 level at the non injecting contact.

Fig.4.3 depict the density of states for rubrene thin film. The order of magnitude is almost the same for all three samples and DOS diminishing with increasing of Fermi energy and exponential trend, as predict by theory.

4.4 Rubrene Field Effect Transistor

A possible application testing the electrical transport properties of rubrene thin film is a transistor structure build on SiO_2. Here is shown the characterization of field effect transistor. This FET is composed by rubrene thin film upon a silicon oxide substrate. Sample AS1306a with thickness $h = 45nm$, contacted on top by two coplanar gold pad and bottom (gate) with silver paint. A layer of SiO_2 is removed by fluoridic acid.

The device was characterized in air and vacuum to compare two trends. Measurement performed at room temperature. Vacuum level around $100mmTorr$.

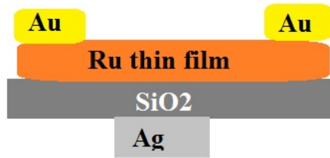

Figure 4.4: Schematic drowning of rubrene FET. Gold contacts are source and drain and silver contact is gate

Here is reported the FET trend at room temperature to verify correct device's function. In following graph is depicted transcharacteristic curves at various drain-source voltage. In characteristic mode is fixed gate voltage and source-drain bias as variable.

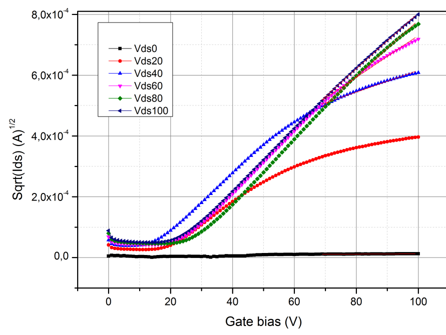

(a) IV curve at fixed drain-source bias and variable gate voltage

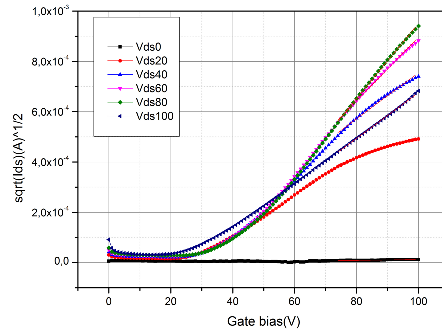

(b) and in vacuum

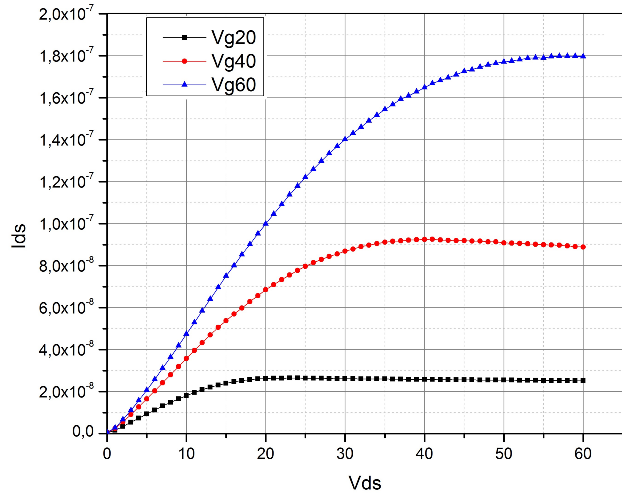

Figure 4.5: IV characteristic in air

In fig.4.5 we note the expected behavior of a transistor in characteristic mode.

After the previous IV curves we repeated the same measurements changing temperatures. Sample cooled by liquid nitrogen inserted in a vacuum chamber and successively heating for Joule effect with a circuit posed below our sample.

For gate voltage $Vg = 0V$ we collected the following curves:

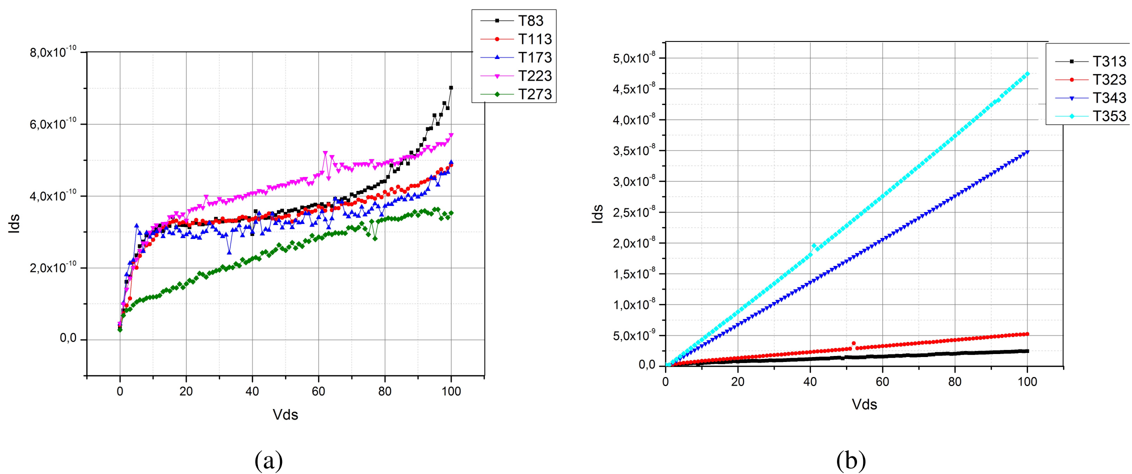

Figure 4.6: field effect transistor IV characteristics when Vg=0 at different temperatures

Setting gate voltage value to -20V:

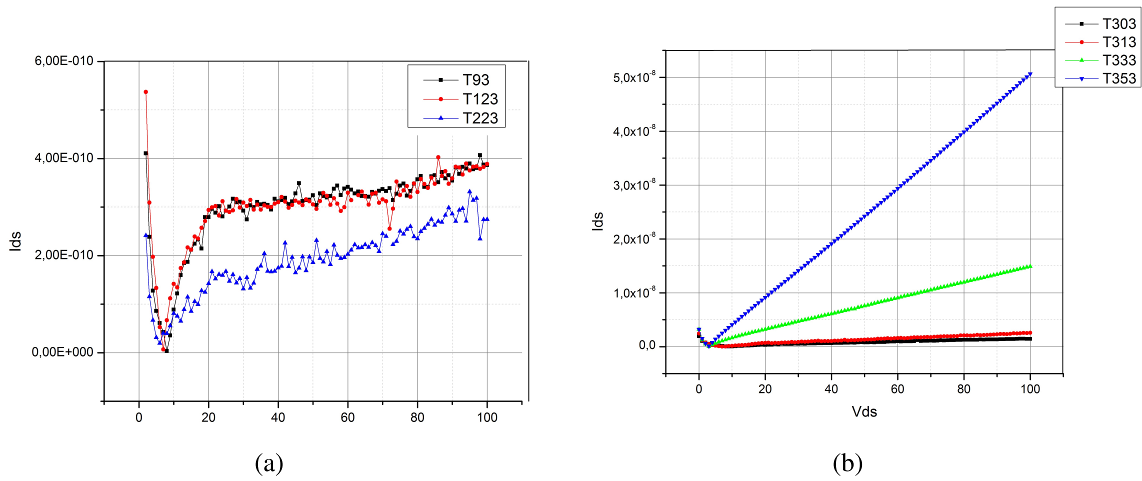

(a) (b)

Figure 4.7: IV charcateristics at $Vg = -20$

There are two different graph because currents are strongly dependent of temperature and in only one it's impossible distinguish curves at low temperatures.

Setting $Vg = -40V$ obtain:

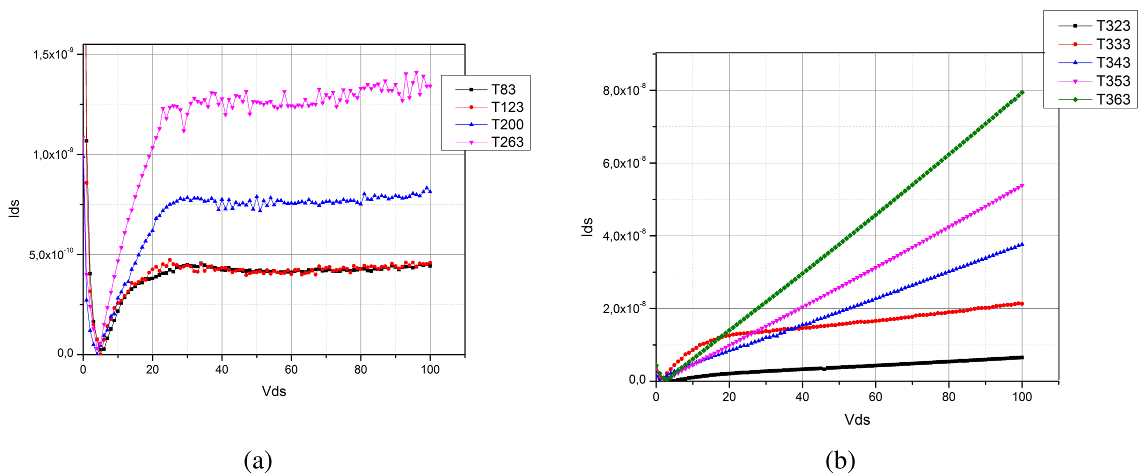

(a) (b)

Figure 4.8: IV charcateristic at $Vg = -40V$ at several temperatures

At gate bias equal to $V_g = -60V$:

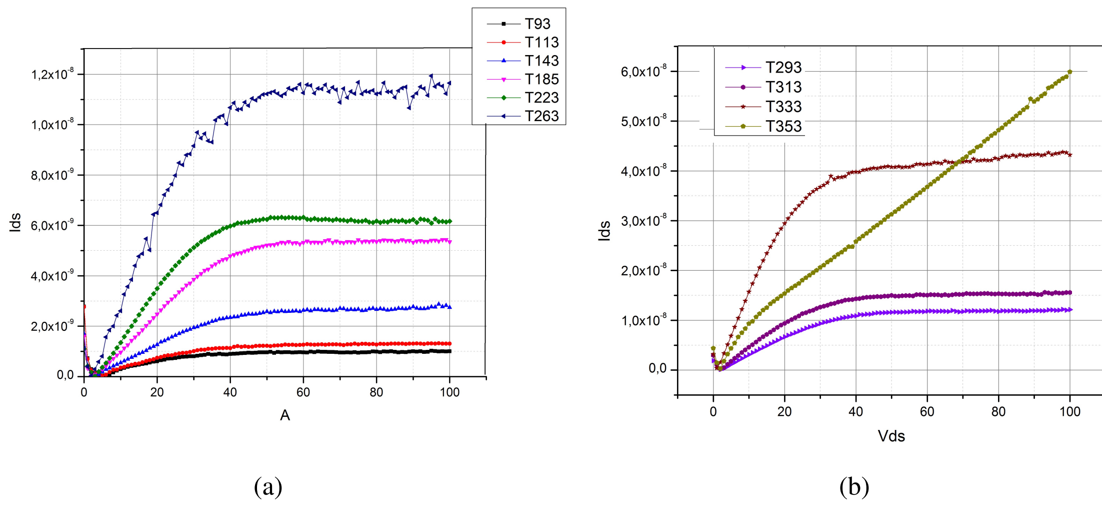

(a)

(b)

Figure 4.9: IV characteristics at $V_g = -60V$ different temperatures

Increasing gate voltage and arriving at $V_g = -80V$:

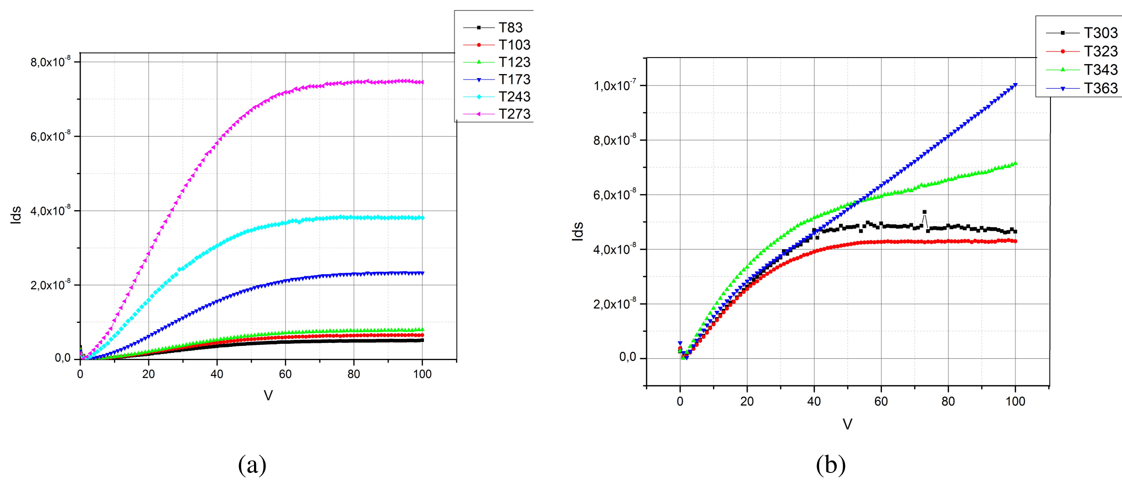

(a)

(b)

Figure 4.10: IV characteristic at $V_g = -80V$ various temperatures

At least it's reported curves at gate voltage equal to $V_g = -100$:

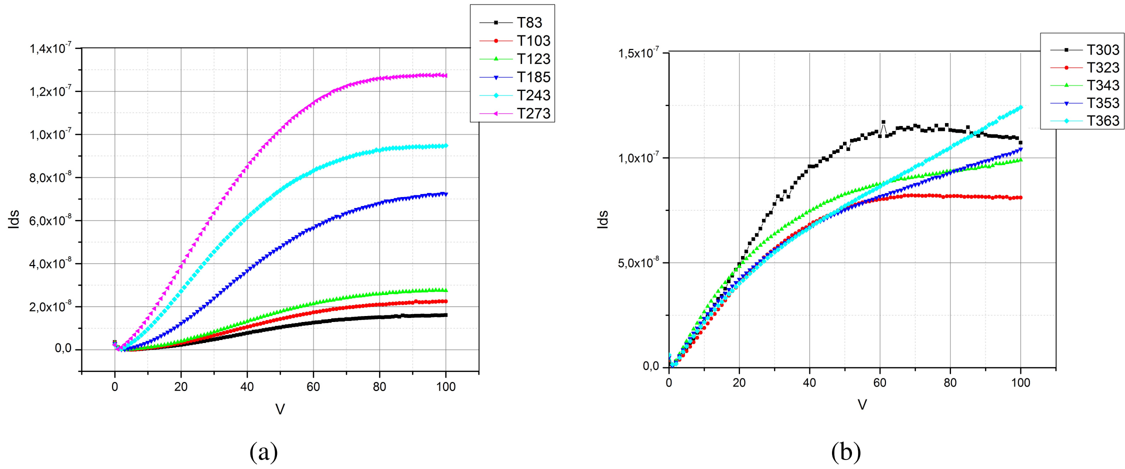

(a) (b)

Figure 4.11: IV characteristic at $V_g = -100V$

This analysis report the behavior of a rubrene FET at various bias and temperatures. We note that with increasing gate voltage the curves are more regular and follow better transistor characteristics. At high T curves tend to be linearized, probably for thermal effects. Studying transistor in transcharacteristic mode, we noted an hysteresis in the curve. Report graph at $Vds = -60V$. IV curves collected in two step, from $0 to 100V$ and from $100 to 0V$. Possible causes of this effects are the interface states due to lattice mismatch between rubrene and SiO_2.

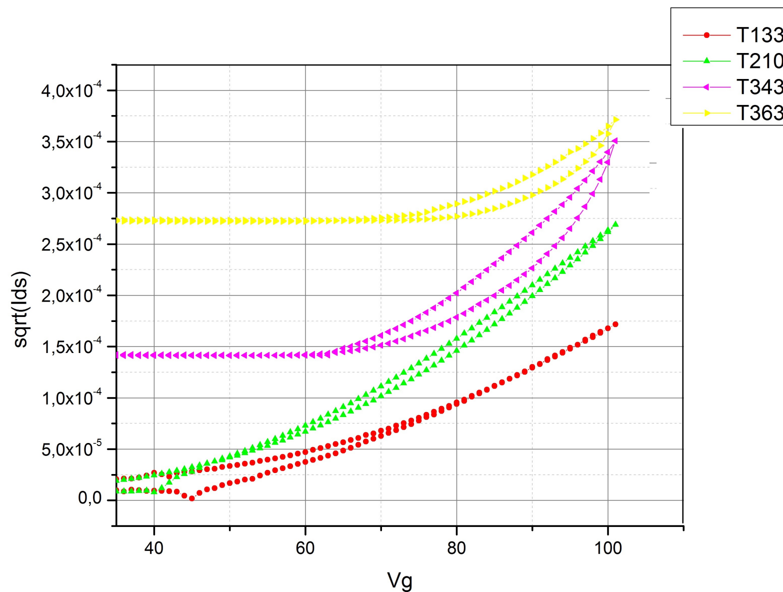

Figure 4.12: IV transcharacteristic at fixed drain-source bias and different temperatures. On y axes is plotted the root square of current

4.4.1 Mobility

Starting from transcharacteristics experiments collecting drain current, we extrapolated mobility as temperature function [26].

The results:

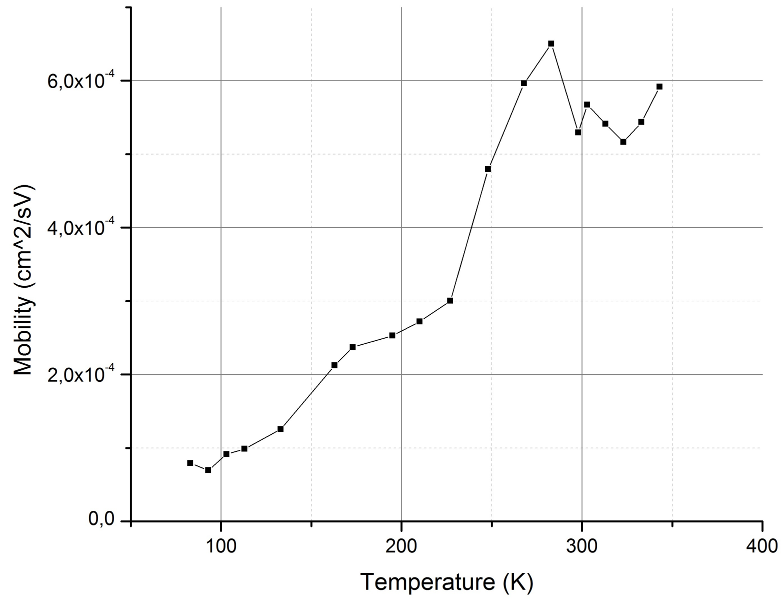

(a) mobility vs. T for $V_{ds} = -60V$

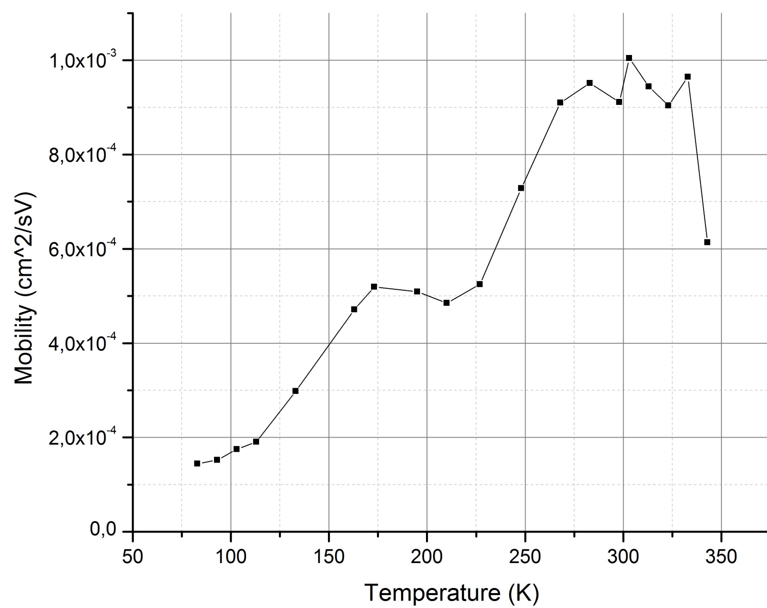

(b) mobility vs. T for $V_{ds} = -100V$

Mobility equation is

$$\mu = \frac{2 \cdot slope \cdot L}{C \cdot W} \tag{4.1}$$

Where C the capacitance oxyde-seconductor in this case is $6.9\frac{\eta F}{cm^2}$, contact width $W = 2.94mm$ and channel lenght $L = 140\mu m$.

It's clear that transport is hopping rather band like from graph. We expected the mobility started from high value at low T and decreased with temperatures.

One of possible reasons may be a strong effect of contact resistance. To try to evaluate contact resistance is used transmission line model briefly illustrated in next section.

4.4.2 Contact Resistance Effects

To evaluate contact resistance of the sample we tested our sample through the Transmission Line Model. This method consist of depositing a metal grid pattern of unequal spacing L_i between the contacts. Each resistor changes only by its distance L_i between two adjacent contacts, as shown in fig 4.14 and it can be expressed by

$$R_i = \frac{\rho_s L_i}{W} + 2R_c \tag{4.2}$$

Then, by plotting the measured resistances as a function of the contact spacing L_i and according to Eq. 4.2, the layer sheet resistivity ρ_s and the contact resistance at $L_i = 0$ respectively that is

$$\begin{aligned} Slope &= \frac{\rho_s}{W}; \\ R_i(intercept) &= 2R_c; and \\ |L_i(intercept)| &= 2L_T. \end{aligned} \tag{4.3}$$

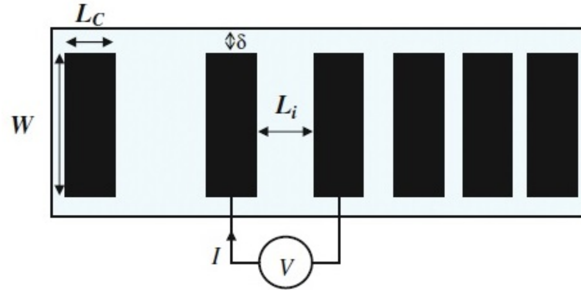

Figure 4.13: transmission line model (TLM) test structure

Resistivity contact (ρ_c) is a parameter with more generalized feature given by:

$$\rho_c = R_c W L_T. \tag{4.4}$$

In case of planar resistor, model needs the concept of transfer length L_T which is shown in fig and is equal to:

$$L_T = \sqrt{\frac{\rho_c}{\rho_{sc}}} \tag{4.5}$$

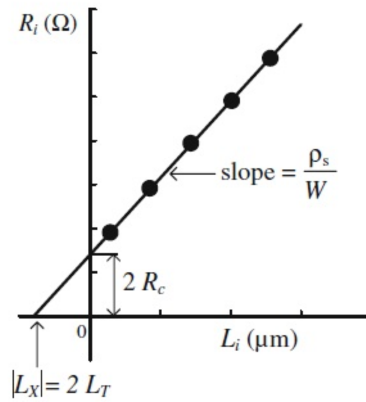

Figure 4.14: Determination of the sheet resistivity and characterization of the contact using TML test structure

Where $\rho_s c$ is sheet resistivity of semiconductor under contact, and this is equal of the sheet resistance between the contacts, then Eq. 4.5 is a correct expression for the transfer length. Substituting R_c from eq 4.4 into 4.2 obtain:

$$R_i = \frac{\rho_s}{W}(L_i + 2L_T) \tag{4.6}$$

TLM method has the big advantage in the ability to give both crucial parameter: resistivity ρ_c of semiconductor contact layer and the contact resistance R_c.

The simple way to take out that physical quantities is done at the expense of brutal assumption that the sheet resistance under contact must be equal to the sheet resistance between the contacts [27].

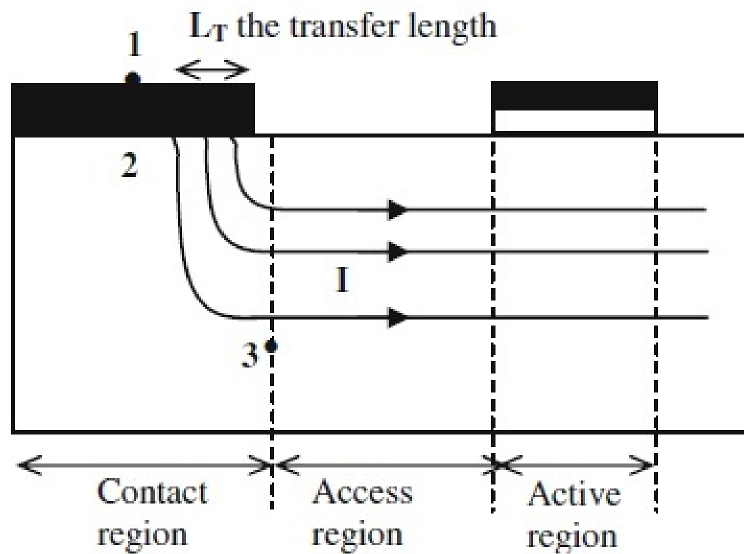

Figure 4.15: Planar contact metal-semiconductor

4.4.3 Contact Resistance results

Sample AS13102-103d is used to perform R_c measurements. The sample has thickness of $50nm$ and three different channel length, respectively of $40, 60, 90\mu m$ obtained shadowing sample with 3 different wires during gold evaporation. Electrical characterization is collected at different temperatures. Our results **channel lenght** $L = 40\mu m$:

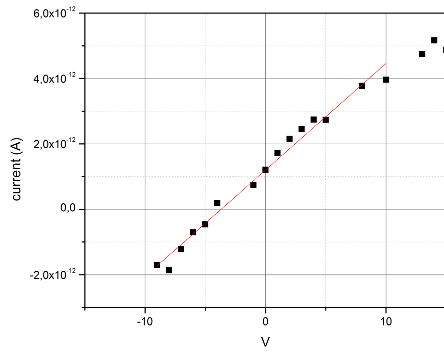

(a) $L = 40\mu m$ at $T = 190K$

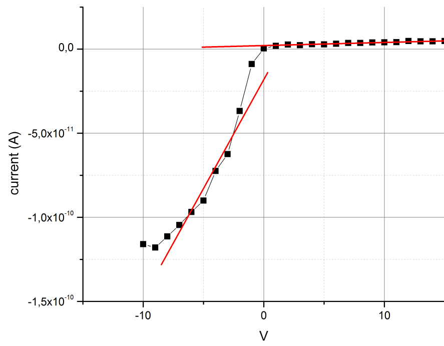

(b) $L = 40\mu m$ at $T = 210K$

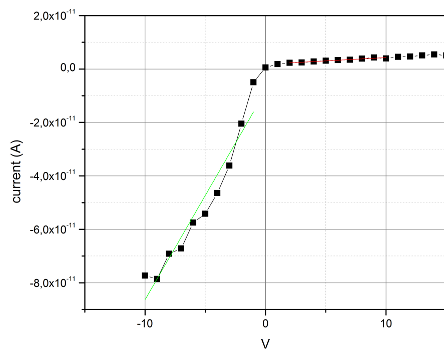

(c) $L = 40\mu m$ at $T = 230K$

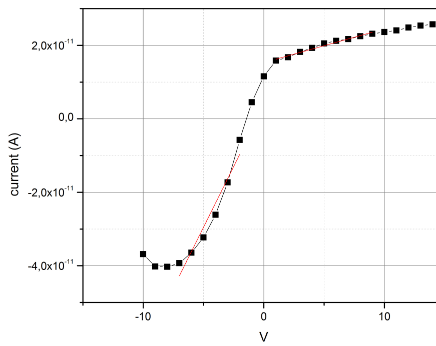

(d) $L = 40\mu m$ at $T = 270K$

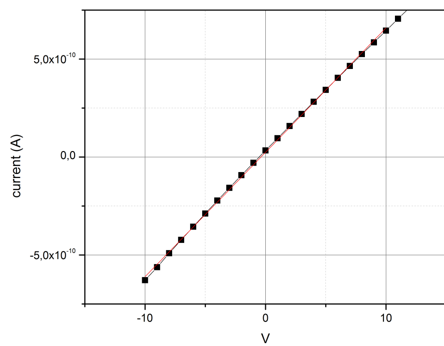

(e) $L = 40\mu m$ at $T = 320K$

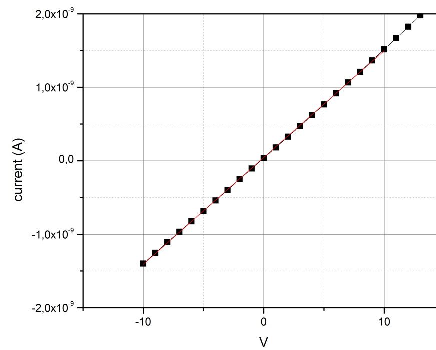

(f) $L = 40\mu m$ at $T = 340K$

Results for **channel length** $L = 60\mu m$:

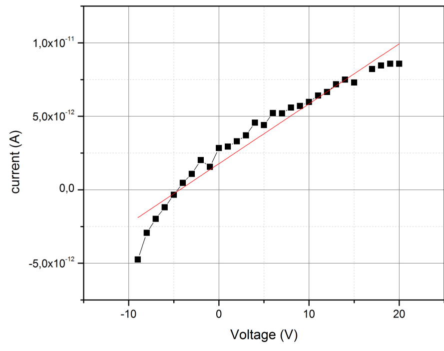

(g) $L = 60\mu m$ at $T = 180K$

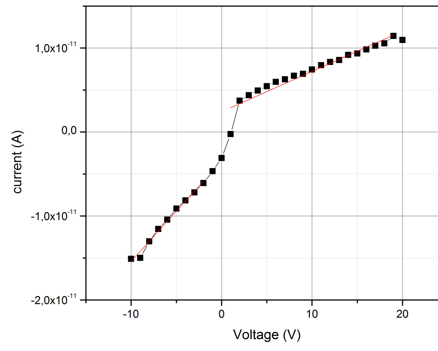

(h) $L = 60\mu m$ at $T = 240K$

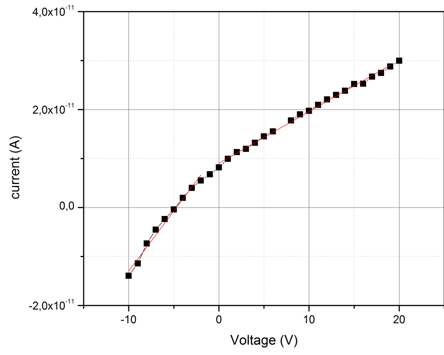

(i) $L = 60\mu m$ at $T = 270K$

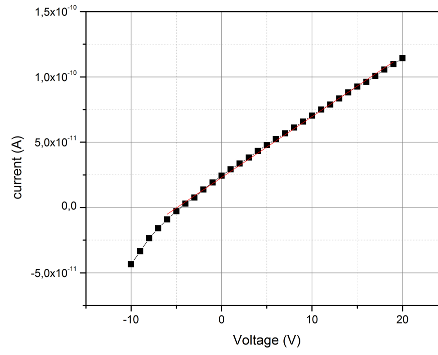

(j) $L = 60\mu m$ at $T = 300K$

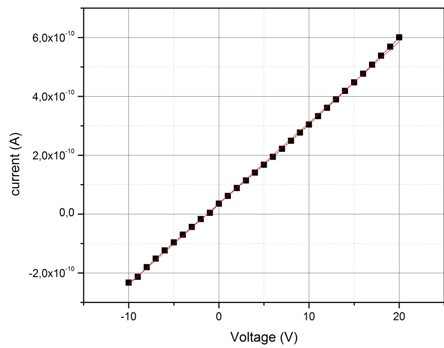

(k) $L = 60\mu m$ at $T = 320K$

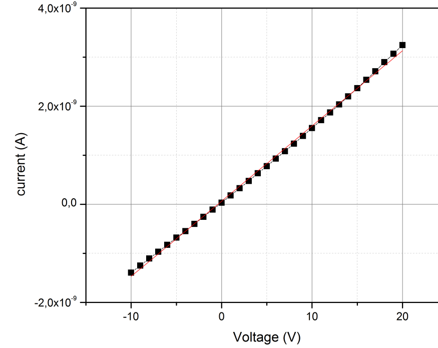

(l) $L = 60\mu m$ at $T = 350K$

Results for **channel length** $L = 90\mu m$:

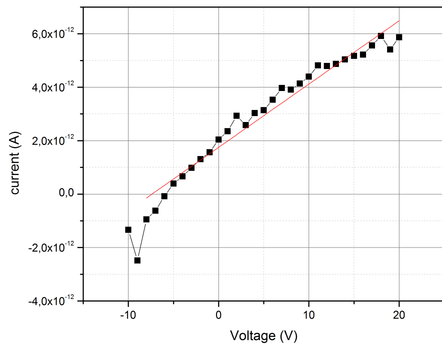

(m) $L = 90\mu m$ at $T = 150K$

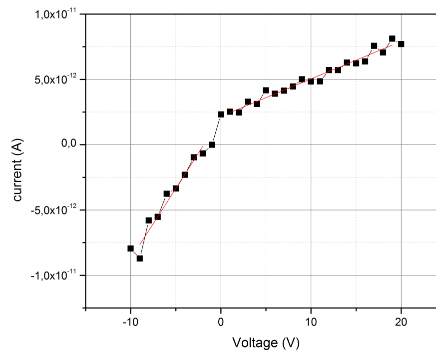

(n) $L = 90\mu m$ at $T = 230K$

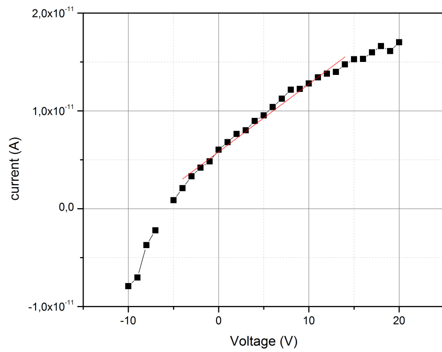

(o) $L = 90\mu m$ at $T = 270K$

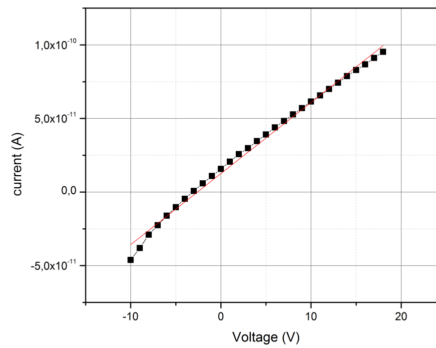

(p) $L = 90\mu m$ at $T = 300K$

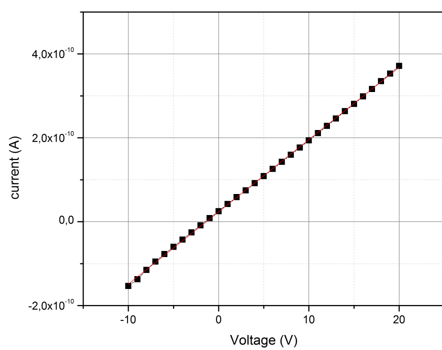

(q) $L = 90\mu m$ at $T = 320K$

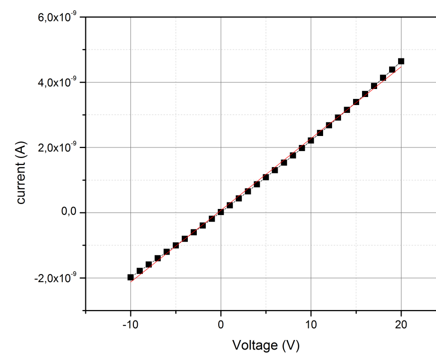

(r) $L = 90\mu m$ at $T = 350K$

In a temperatures range from $190K$ to $270K$ our sample has a behavior like a Schottky diode, present in all three channel. Upon and above this interval, IV characteristics are almost linear.

We don't know the answer yet. Maybe is due to some defects within material which affect whole sample. These defects, probably, generate deep levels inside energy gap and the occupancy levels varies with temperatures. Knowing that Fermi level moving into gap with T, and when E_F crosses the defect band it is emptied and will be create space charge region which gives rise to a rectifier junction (Schottky barrier), as illustrate in fig 4.16.

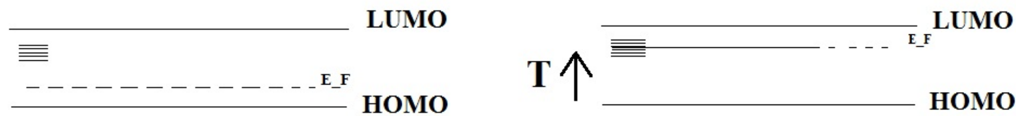

Figure 4.16: Simplified scheme of crossing between defect band with Fermi level which moves with temperature

Just for curve at $T = 320K$ using TLM is possible extract value of contact resistance: From graph we look that contact resistance is negligible within errors bars.

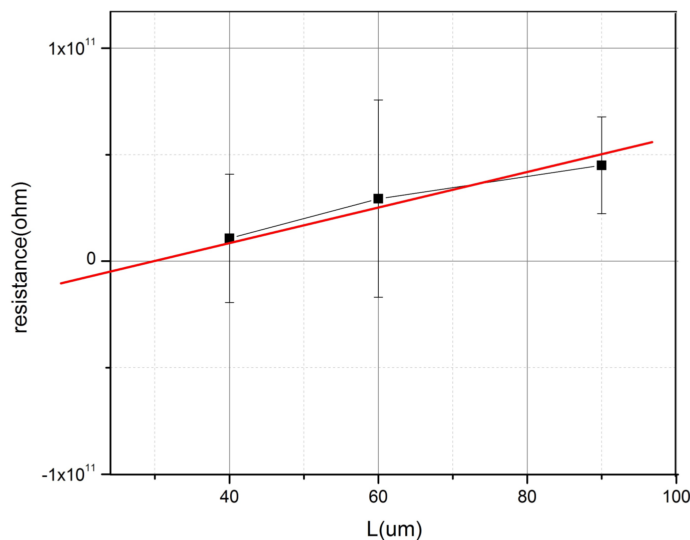

Figure 4.17: $T = 320K$ half value of intercept with y-axes is R_c

4.4.4 Annealed thin film IV characteristic

To avoid Schottky effects we carried out an annealing process to improve the matching between gold and crystal. After deposition of gold we heating rubrene thin film at 60^oC for 10 minutes.
IV characteristics at different temperatures lead to the following results.

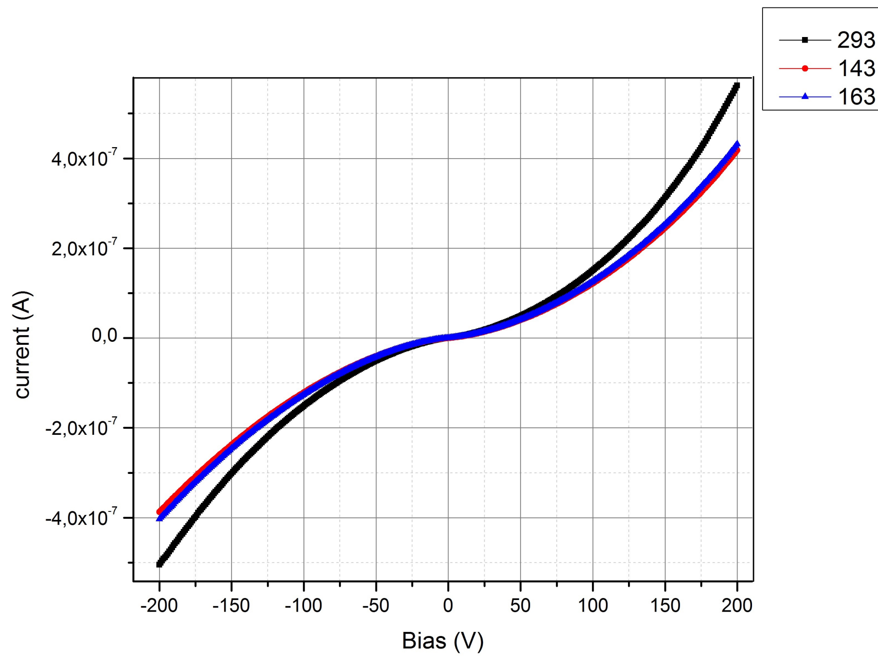

Figure 4.18: AS1369a. IV characteristic at different temperatures. Symmetry provide good gold contacts.

Symmetrical curve in Fig. 4.18 tells us that the current in this case is limited by the bulk of the crystal; that is, the current is bulk limited rather than contact limited. The linear (Ohmic) regime at very low bias also indicates that the nonlinear Schottky barrier formed at the metal-semiconductor interface is in this case negligible [16].

Other measure were accomplished only for positive bias at different temperatures.

These characteristics do not reach trap fill limit to not stress excessively our sample. So is possible investigate the density of state for each temperatures. As illustrated by SCLC theory in chapter 4 the DOS is obtained using an algorithm written in Pyhton by doc. Andrea Ciavatti.

Graphs depicted density of states vs activation energy at different temperatures.

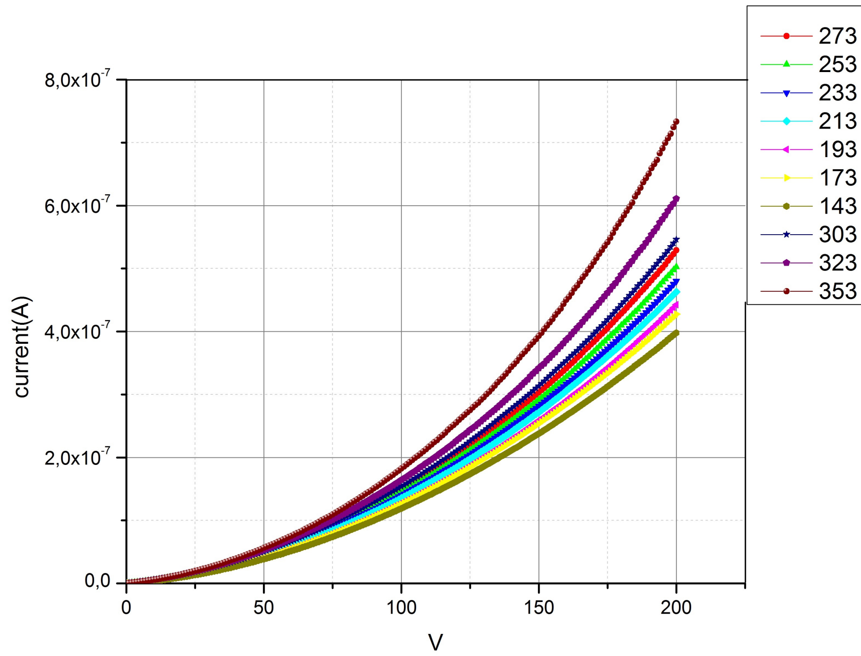

Figure 4.19: Comparison of current vs applied voltage for a rubrene thin film not transfered at several temperature

The density of states have an exponential trend as expected. This graphs are more linear and regular with respect to fig.4.3. The substantial difference is the range of applied voltage. In this case sample do not overcome 200V. For the same reason is possible to note a difference about one order of magnitude of Fermi energy with respect to values reported in Fig. 4.3. This analysis put on evidence a diminishing of two order of magnitude with increasing temperatures.

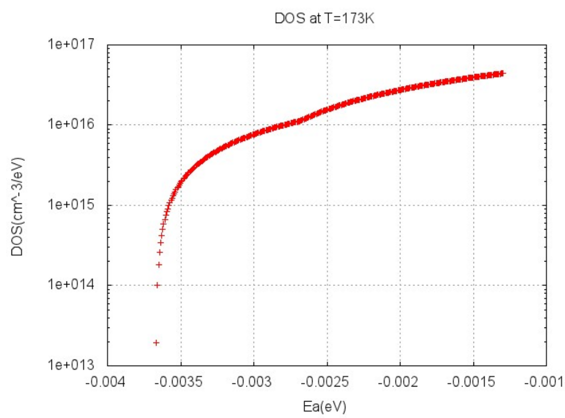

(a) $T = 173K$

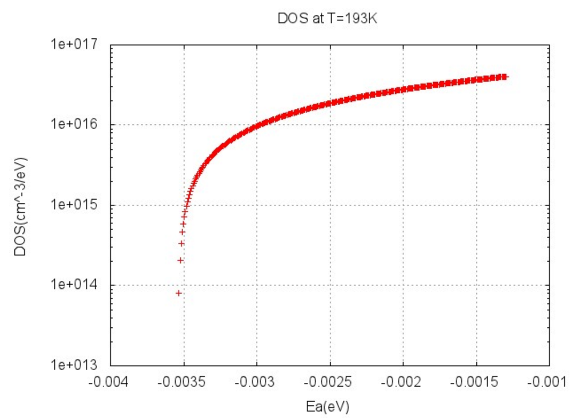

(b) $T = 193K$

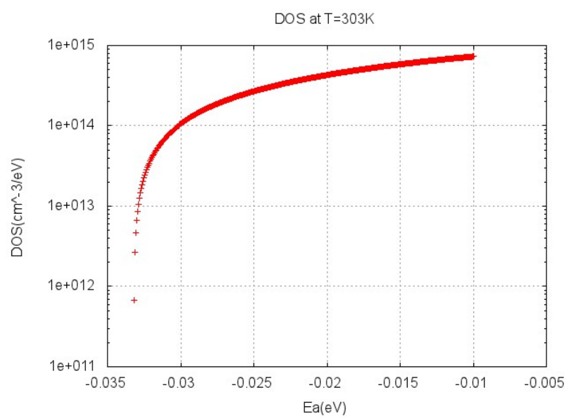

(c) $T = 303K$

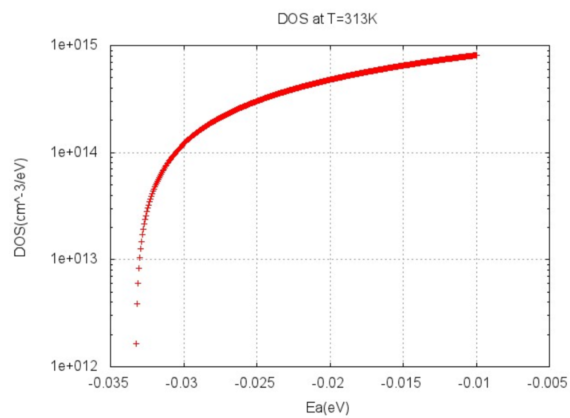

(d) $T = 313K$

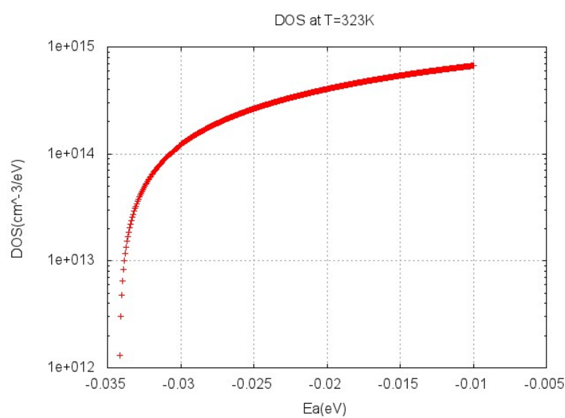

(e) $T = 323K$

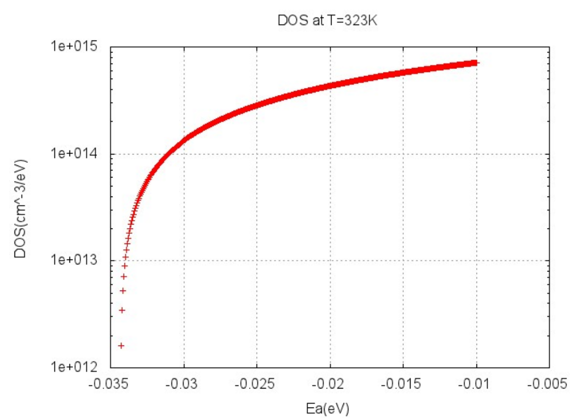

(f) $T = 333K$

Figure 4.20: Density of states vs. activation energy in semi-log scale at fixed temperature keeping constant during entire measurement

Chapter 5

Photocurrent

The experimental technique named photocurrent spectroscopy is based on the optoelectronic phenomenon of photoconductivity, i.e. the increase of the electrical conductivity of a material when it is exposed to electromagnetic radiation (visible light, ultraviolet light, infrared light, or gamma radiation). Essentially the physical phenomenon of photoconduction in a semiconductor is based on the absorption of a photon by an electron (internal photoelectric effect). If the photon energy is high enough, the photon absorption causes the excitation of the electron across the forbidden bandgap i.e. from the valence band to the conduction band in inorganic semiconductors, and from HOMO to LUMO in organic semiconductors. Also transition from impurity levels eventually present in the bandgap can occur and they correspond to absorption of radiation with energy lower than the bandgap. It should be noted that, since in an organic molecule several anti-bonding orbitals are present (LUMO representing the lowest one), the absorption of radiation with energy higher than the bandgap corresponds to transitions between higher energy levels for an organic semiconductor. Thus, when electromagnetic radiation is absorbed by a material such as a semiconductor, the number of free electrons and holes changes and raises its electrical conductivity. In fact, when a load resistor is used in series with the semiconductor and a bias voltage is applied to the circuit, a voltage drop across the load resistors can be measured as the change in electrical conductivity of the semiconductor varies the current owing through the circuit. This current is named photocurrent. The conductivity of a semiconductor in darkness condition can be expressed as function of electron end holes concentration, indicated with n0 and p0 respectively, as follows:

$$\sigma = e(n\mu_n + p\mu_p) \tag{5.1}$$

where e is the electronic charge and μ_n and μ_p are the electrons/holes mobility. When the material is exposed to an electromagnetic radiation with $h\nu \geq E_g$ (E_g is the energy gap of semiconductors), the absorption of a photon results in the generation of an electron-hole pair and thus in an increase of the conductivity:

$$\sigma + \Delta\sigma = e[(n+\Delta n)\mu_p + (p+\Delta p)\mu_p] \tag{5.2}$$

Therefore, the current density $J = \sigma E$, where E is the electrical field applied, increase to the value:

$$J = (\sigma + \Delta\sigma)E = J_{bulk} + J_{ph} \tag{5.3}$$

Through the measurement of the variation of J in the sample is therefore possible to detect the light absorption by the material. Indeed, when a photon is absorbed by an organic semiconductor the formation of an electron-hole pair is not so easy as for inorganic materials. In fact the absorbed photon can be emitted immediately by the material or an exciton can be created. An exciton is a bound state of an electron and a hole, which in inorganic semiconductors has a weak binding force (1 meV to 20 meV), and so it can easily dissociate forming an electron-hole pair, while in organic semiconductors the excitonic bond is stronger (between 100 eV and 300 eV). Typically, the presence of two different polaronic states on distinct molecules is required in order to generate the photocurrent signal. Also, once generated, the electron-hole pair has an average life time τ , at the end of which the charge carriers are not more available for conduction. τ is affected above all by recombination processes due to the presence of trap levels in the forbidden gap. The recombination processes can decrease τ until a critical value, under which no photocurrent signal can be detected. Also, traps can bond charge carrier only for a certain time (which depends on the energy associated to the trap in the band gap) but also in this case the macroscopic effect will be a decrease in the detectable photocurrent due to charge trapping. [28][29]

All photocurrent-based techniques have in common that they are highly sensitive spectroscopic techniques that allow the detection of small concentrations of dopants, defects or charge-transfer complexes in a material.

In many discussion of photoconductivity it is possible to make two simplifying assumptions:

- the conductivity is dominated by one of the carriers so that the contribution of the other can be effectively neglected.
- the crystal staysneutral during the photoconductivity process without a build-up of appreciable space charge in the crystal: i.e., $\Delta p = \Delta n$

The lifetime of photoexcited carriers is the key parameter for an understanding photoconductivity. There are several quantities indicates with term ′ lifetime′. Let see them in more details.

We distinguish various type of lifetime:

- FREE LIFETIME: is the time that an excited electron spends in the conduction band, or the time that an excited hole spends on the valence band. The free lifetime of a charge carrier can be terminated by recombination or interrupted if the carrier is trapped.
- EXCITED LIFETIME: is the total time the carrier is excited between the act of excitation and the act of recombination. The excited lifetime includes any times that the carriers may spend in traps; is therefore longer than the free lifetime.

- PAIR LIFETIME: is the free lifetime of an electron-hole pair. If either electron or hole is captured, or is Extracted without replenishment, the lifetime is terminated.
- MINORITY-CARRIER LIFETIME: is the free lifetime of the minority carrier, i.e., the carrier which makes the minor contribution to the conducivity.
- MAJORITY-CARRIER LIFETIME: is the free lifetime of the majority carrier [28].

Recombination Recombination determines the lifetime of the photoelectrons (or holes) and it is the reverse of thermal excitation.
Recombination is not so much due to an electron and a hole combining directly and thus eliminating each other, but a variety of processes which involve a kind of intermediate state called **traps**.

If the electron or holes falls into such a trap, it is, for a finite average time interval, no longer free and its probability o recombination with carrier of opposite sign is increased. However, there is also a finite probability that the carrier may escape from the trap. Both of probabilities depend in the enrgy level of the trap and the mean energy of the carrier. Traps was usually born by crystal imperfections, dislocations, grain boundaries, and the surface of the material. The lifetime of a carrier may be rewritten as:

$$\tau = \frac{1}{vsn} \tag{5.4}$$

where v is the mean velocity of charge carrier, s the collision cross section of the trap (determined by its energy and called ´capture cross section´), and n is the concentration of the traps.
The photocurrent is:

$$I_{ph} = \frac{eF\tau}{T_r} \tag{5.5}$$

e is the electronic charge, F is the of carrier excited into the conduction band per second. In the considered sample the distance between two electrodes is L and there is an applied voltage V. T_r is the transit time, in other word:

$$T_r = \frac{L^2}{V\mu} \tag{5.6}$$

The mobility is related to lifetime by:

$$\mu = \frac{e\tau}{m} \tag{5.7}$$

The photoelectric effect produces a free electron-free hole pair. One kind of there charge carriers (in many cases the free holes) is rapidly trapped, but the remaining carrier moves under the influence of external applied field. As soon as one electron leaves the semiconductor at the anode, another enters from the external circuit, at the cathode, and therefore current flows.

The recombination process may be either radiative or nonradiative. A radiative recombination involves the conversion of the energy liberated by recombination into a quantum of radiation which then is either reasorbed in the crystal or emitted. Nonradiative recombination does not result in the emission of electromagnetic radiation. The energy becomes heat. This process occur in a different step, involving intermediate energy levels. Lifetime is usually larger than radiative recombinations.
Energetically, the traps must be regions of localized positive potential for electrons, and regions of local negative potential in order o attract holes.. In the vicinity of trap there is a local band deformation which creates an energy minimum. The traps are usually closely coupled to the lattice, a number of discrete energy levels exist within the trap. The time that an electron passes inside the trap depend on the depth of the trap, that is, on the difference between the bottom of the conduction band and the energy level occupied by the electron within the trap , and also the initially energy of the electron.
The distance between the lowest energy level within a trap for electrons and the bottom of the conduction band may be comparable to kT, in which case we speak of a shallow trap. Conversely, the depth of the trap thus defined may be large to compare with kT, then the trap is called deep trap. Shallow traps are nearly always filled and can be considered to be in thermal equilibrium with the conduction band. Electrons trapped in shallow traps are quickly released again. However, electrons may spend considerable times in the deep traps. Once captured, the probability of the electron accumulating enough energy to escape from the trap is not very larger than the probability for an electron to be excited across the energy gap in intrinsic conduction. Another important effect in photoconctivity is played by the crystal surface states which affect even the shape of the spectral response curve. An ideal solid surface represents a lattice discontinuity. The energy band structure show profound distortions at the surface. The presence of surface must give rise to a series of localized energy levels which do not exist in the bulk of the crystal. There is the formation of dangling bonds. A dangling bond represent a region from which an electron is missing. At the surface the conduction properties are profoundly different with respect to the bulk. The surface states will be fully ionized except at very low temperatures. If the bulk of semiconductor is $n-type$ the surface in $p-type$. This is called *inversion layer*. The concentration of holes in the surface region is greater than in the bulk. The excess holes in acts as electron acceptors, these electrons are not free, they are trapped on the surface. On $p-type$ semiconductor an *accumulation layer* builds up, indicating that the concentration of majority carriers is substantially higher in the surface region than in the interior. The number of surface states, known as *Shockley states*, in a clean material should be of the same order as the number of surface atoms. Any real surface in air will be covered by on oxide layer, at least some tens of Ångstrom thick. This oxide layer also give rise to surface states which act as traps. Moreover, the presence of oxide layer give rise to an interface between the semiconductor as such and the oxide, also giving rise to surface states. In general, surface states mat be slow states, i.e., energy states which are slow in coming to equilibrium with the free carriers. Or fast states, in which equilibrium between them and the free carriers is established very quickly. They are strongly affected by

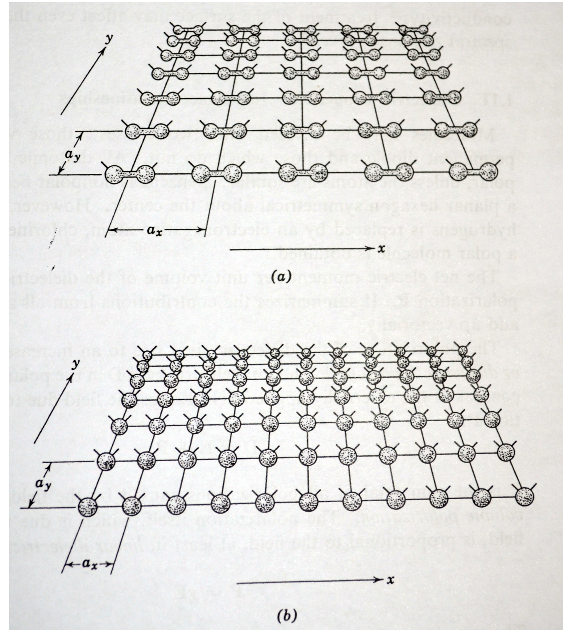

Figure 5.1: Atomic arrangements in semiconductors surface. Diagram (a) represents an idealized germanium lattice plane. The lattice plane, as it would appear within the bulk of the solid, is shown in (b) for comparison. The lattice spacings in the x and y directions are equal in the bulk, but $a_x = 2a_y$ in the surface. [30]

the surrounding atmosphere. Because both slow and fast states acts as traps, the density of traps in the surface is always very much higher than the bulk concentration of traps [30].

5.1 Experimental Results

For the first time we performed photocurrent on rubrene thin films. The aim of these measurements is to obtain rubrene energy gap, crystalline order and eventually differences depending by sample thickness. Our starting point is work done in [7] and [31].
Photoconductivity experiments were performed in our laboratory with apparatus reported in Chapter 2. Najafov et al. in [7]developed a highly sensitive trap characterization technique based on wavelength and polarized-resolved photocurrent excitation spectroscopy of single crystalline organic semiconductors.
They correlated photoconductivity with light absorption coefficient on three different rubrene crystals.

- pristine high-purity rubrene with negligible trap density and a large built-in surface conduction channel;
- medium-purity crystals, in which the built-in surface conduction channel is suppressed by traps (the so-called, trap-dominated crystals);

- intentionally photo-oxidized crystals, in which the trap density can be increased in a controlled fashion.

The method reveals that even a brief illumination of organic molecular crystals in an oxygen atmosphere triggers a long-term oxygen diffusion that continues in the dark and results in formation of oxygen-related traps in the crystal at the length scale $\sim \alpha^{-1}$, where α is the light absorption coefficient. These studies show that oxygen diffusion occurs in the dark without an initial photoexcitation, even if the samples are stored in pure oxygen. They performed measurement on rubrene because of its anisotropic molecular packing then the absorption coefficient $\alpha(\lambda\theta)$ is both wavelength (λ) and polarization angle (θ), dependent. θ is defined as an angle between the polarization of linearly polarized light and the $a-$axes of rubrene fig.**??**. α reaches maxima for polarization along the high-mobility $b-$axis ($\theta = 90^0$) and minima for polarization along the $a-$axis of rubrene ($\theta = 0$).
Vibronic modes of rubrene cause large modulations of α with wavelength (Figure **??**b). This gives the possibility to vary continuously the characteristic light penetration length in the $c-$axis direction according to the Beer–Lambert law in a wide range by changing λ or θ:$\alpha^{-1}(\theta,\lambda) = 1 - 140\mu m$. These properties are used to study the distribution of oxygen-induced traps in rubrene by measuring the photoconductivity, $\sigma(\theta,\lambda)$, which is then compared with $\alpha(\theta,\lambda)$. The thickness of all samples in this study was:$0.5 - 2mm$.

Fig.**??** shows the polarization dependence of the photoconductivity measured under monochromatic photoexcitation in the range of $495 - 580nm$. We can see that in macroscopically thick rubrene crystals, photoconductivity shows small periodic modulations with polarization angle. here these conductivity modulations are always much smaller than the corresponding modulations of the absorption coefficient. The important result is that bulk photoconductivity in pristine rubrene is negligible, and up to 90% of the total photocurrent originates from a long-range diffusion of excitons ($3 - 5\mu m$) and their surface dissociation, which provides a dominant contribution to the photoconductivity.

Figure **??** shows photoconductivity measured in a trap-dominated sample. here modulations of the photocurrent with λ and θ are inverted, i.e., they anticorrelate with the absorption function $\alpha(\lambda,\theta)$.Antimodulation in photoconductivity must arise from carrier trapping.

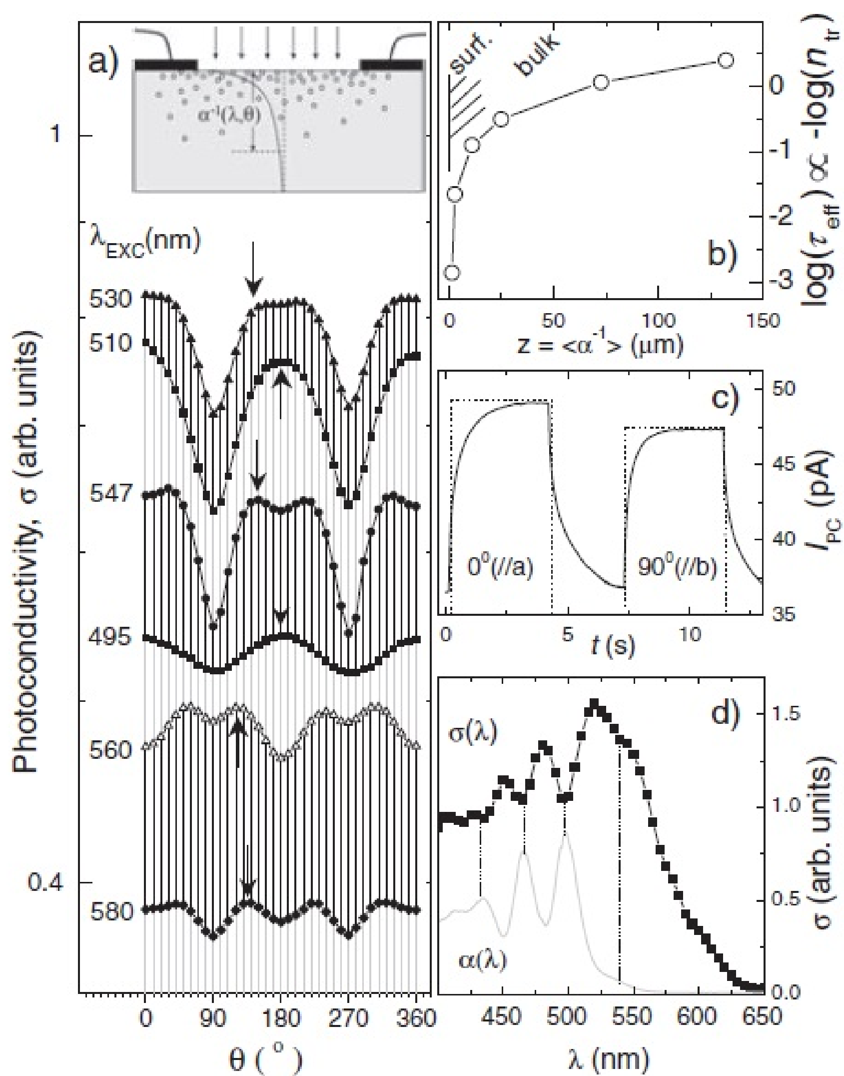

(a) a) polarization dependence of the photoconductivity in pristine (high pure) rubrene crystal at various excitation wavelength. The light is normally incident at the surface of the crystal. b) Absorption coefficient. c) Photocurrent excitation spectrum of pristine rubrene crystals.

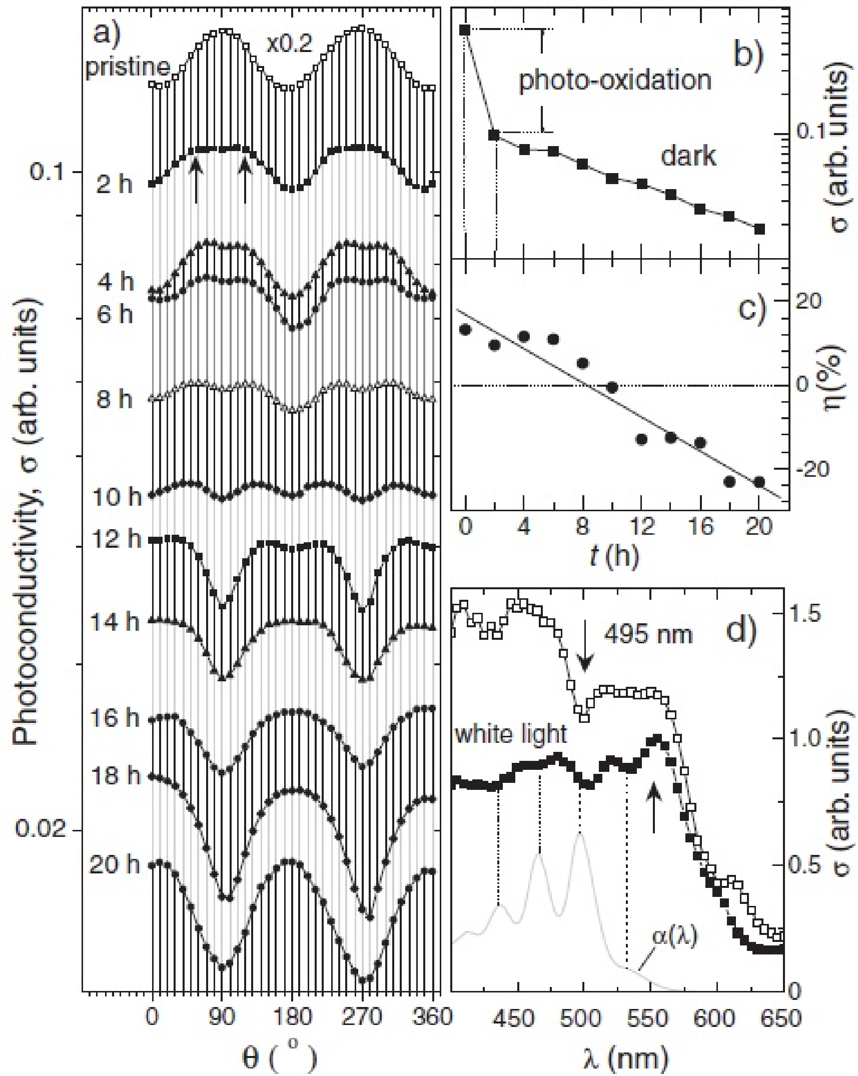

(b) a)Polarization dependence of the photoconductivity in a trap dominated rubrene crystal showing the antimodulated behavior. b) Distribution of trap-limited carrier lifetimes and densities in a trap dominated sample as a function of the depth into the crystal. c) c) Time dynamics of the photocurrent induced by 580 nm rectangular pulsed photoexcitations polarized along a- and b- axes of the crystal. d) A photocurrent excitation spectrum of a trap-dominated rubrene crystal (solid squares) with the absorption spectrum (grey solid line) shown for comparison.

5.1.1 Photocurrent on rubrene bulk and thin films

For the first time we performed photocurrent analysis on thin films to extract energy band gap, E_g, and crystallinity as thickness function and on rubrene bulk to compare with thin films.
Measurement on different sample reported in 5.1

Sample	type	thickness	substrate
Ru2	bulk	$10\mu m$	quartz
AS13104-105a	thin film	$15nm$	free standing
AS13102-103a	thin film	$50nm$	free standing
AS106-107a	thin film	$75nm$	free standing

Table 5.1: Samples used for photocurrent spectroscopy with different characteristics

On samples were deposited gold contact with two different channel length: $50\mu m$ and $90\mu m$ as in fig5.2 . Measurement were performed with two slits of $2000\mu m$ and $250\mu m$.

We collected photocurrent for both channel length and two different slits, comparing results and searching, eventually, differences between two spectrum to reach the best configuration.

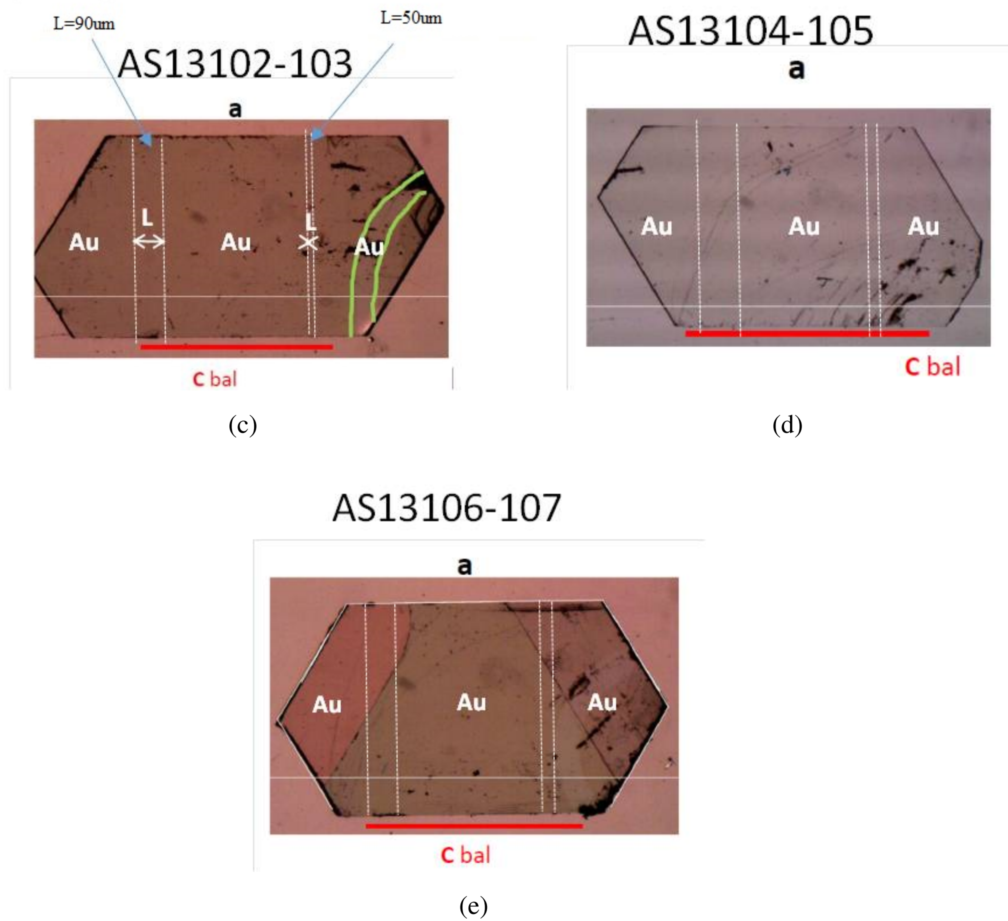

(c)

(d)

(e)

Figure 5.2: Rubrene thin films with two channel length realized to perform photocurrent

For sample with 15nm of thickness the curve is noisy and low clean so did not make measurement with smaller slit. At the beginning we measure photocurrent in two different channels to verify if different values of electric field affects the results. As we can see in Fig.**??**, the maxima and the minima appears at the same wavelengths (or energies). It demonstrates that E does not influence the photocurrent, or maybe that values of electric field for both channel has a very low difference to affect the photoconductivity.
Further analysis consist in a comparison between bulk and three thin films. For $L = 90\mu m$ we obtained:

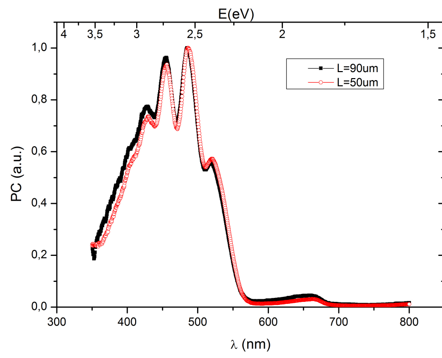

(a) AS13106-107a $h = 75nm$ comparison between two channel length $L = 50\mu m$ and $L = 90\mu m$ and slit of $W = 2000\mu m$

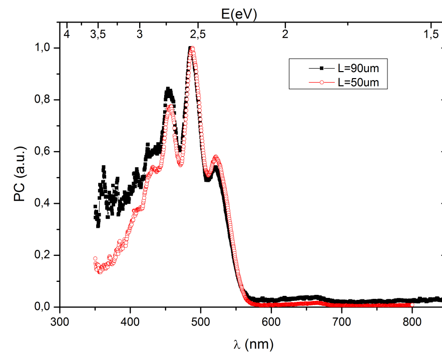

(b) AS13106-107a $h = 75nm$ comparison between two channel length $L = 50\mu m$ and $L = 90\mu m$ and slit of $W = 250\mu m$

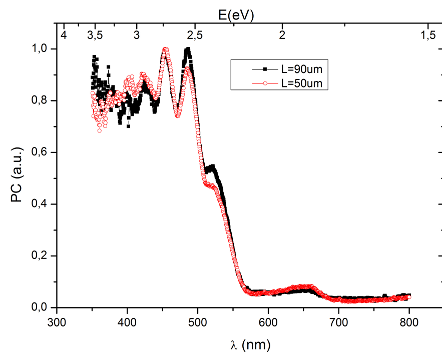

(c) AS13102-103a $h = 50nm$ comparison between two channel length $L = 50\mu m$ and $L = 90\mu m$ and slit of $W = 2000\mu m$

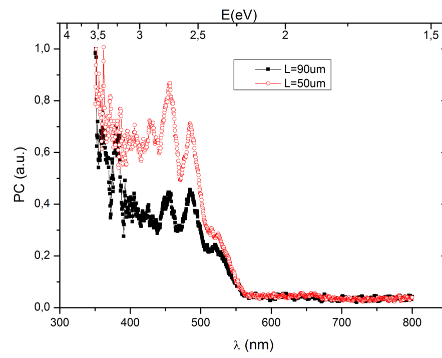

(d) AS13102-103a $h = 50nm$ comparison between two channel length $L = 50\mu m$ and $L = 90\mu m$ and slit of $W = 250\mu m$

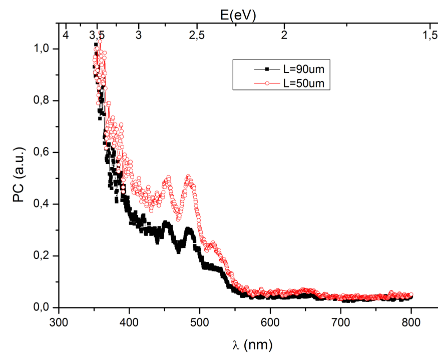

(e) AS13104-105a $h = 15nm$ comparison between two channel length $L = 50\mu m$ and $L = 90\mu m$and slit of $W = 2000\mu m$

For a complete treatment we report also the spectrum collected in smaller channel $L = 50\mu m$:

In fig.5.3 is possible to see that peaks of bulk and thin films perfectly coincides. It may confirm the crystal order of thin films.

In fig5.5 is depicted photocurrent of rubrene bulk, for slits of 2000 and 250 μm, and the spectra of literature [7] of a macroscopically rubrene. Here still we don't have antimodulated trend of our samples with respect to literature spectra, as expected, but just an easy shift toward higher energies.
It is early to give an answer for this behavior, we must perform other measurements. Also we taking in account that this is the first photocurrent experiment made on thin films, so we do not have other data to compare our results. Crystal order is proportional to thickness and the fact that for bulk and thin film peaks coincides give us the confirm that thin films have a good stacking.

From that photocurrent spectrum we extract energy gap reported in table 5.2

h(nm)	Eg(eV)
bulk	2.17 ± 0.02
75	2.21 ± 0.02
50	2.18 ± 0.02
15	2.21 ± 0.02

Table 5.2: Energy gap obtained from photocurrent spectrum for bulk and thin films

Energies gap extracted from photocurrent data are comparable with expectation values reported in literature for microscopically rubrene single crystal.

Further measurement may be carried out changing polarization, from 3V to 18 V to investigate the effect of electric field on photocurrent spectra.

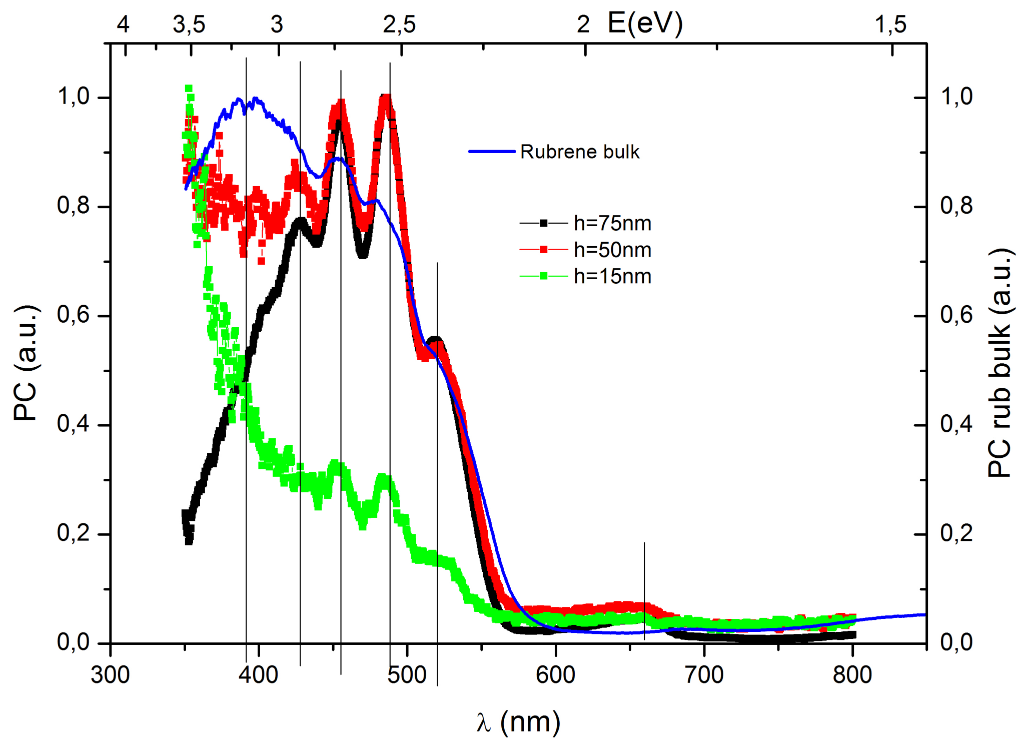

(f)

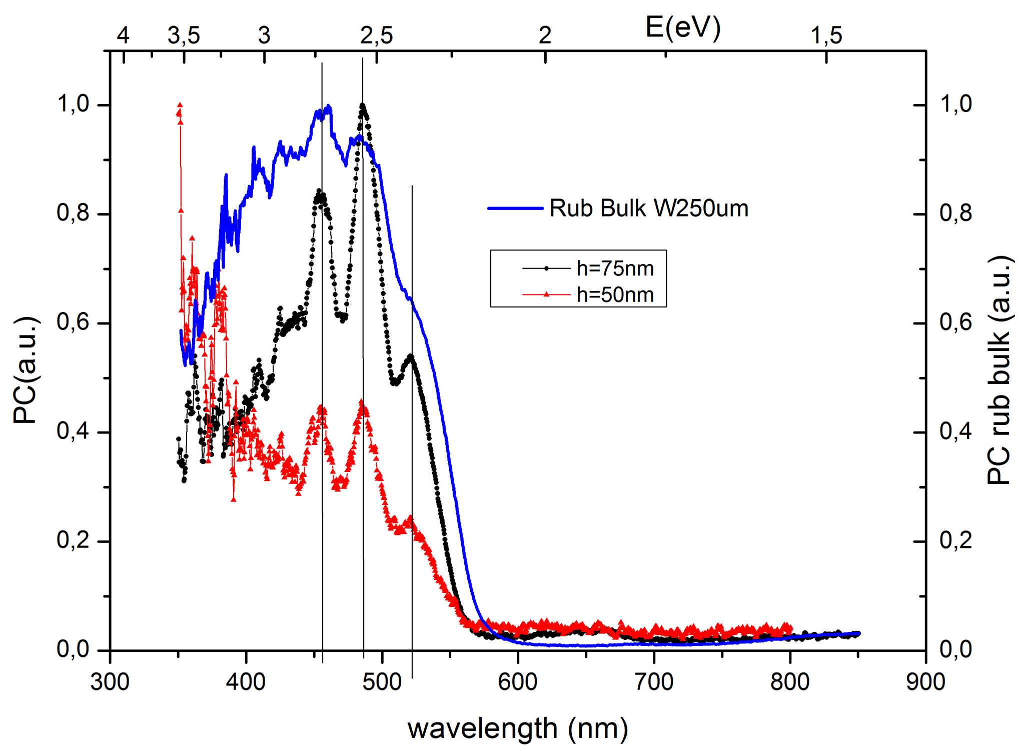

(g)

Figure 5.3: Photocurrent spectra using splits of 2000μm (f) and 250μm(g) channel length $L = 90\mu m$. Rubrene bulk and the three film with different thickness reported on the graph. All curves are normalized

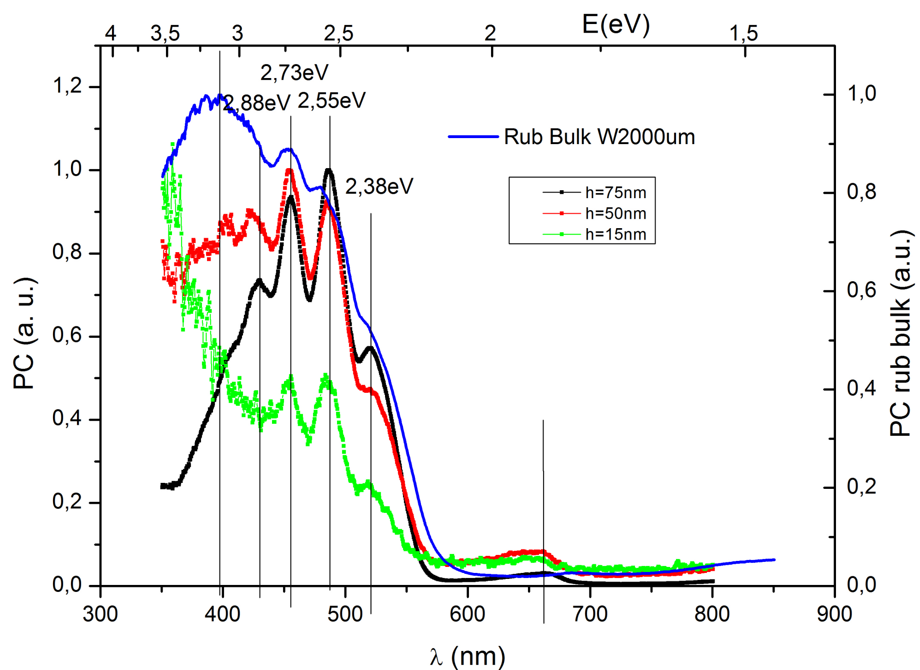

(a)

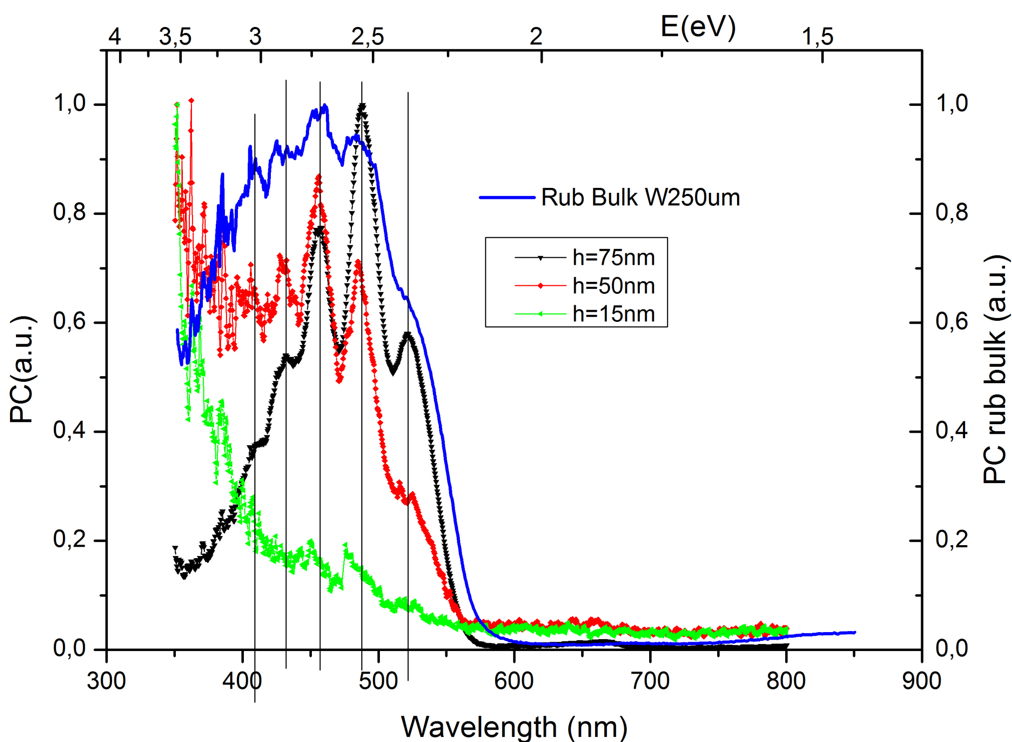

(b)

Figure 5.4: Photocurrent spectra using splits of $2000\mu m$ *(a) and* $250\mu m$*(b) channel length* $L = 50\mu m$*. Rubrene bulk and the three film with different thickness reported on the graph. All curves are normalized*

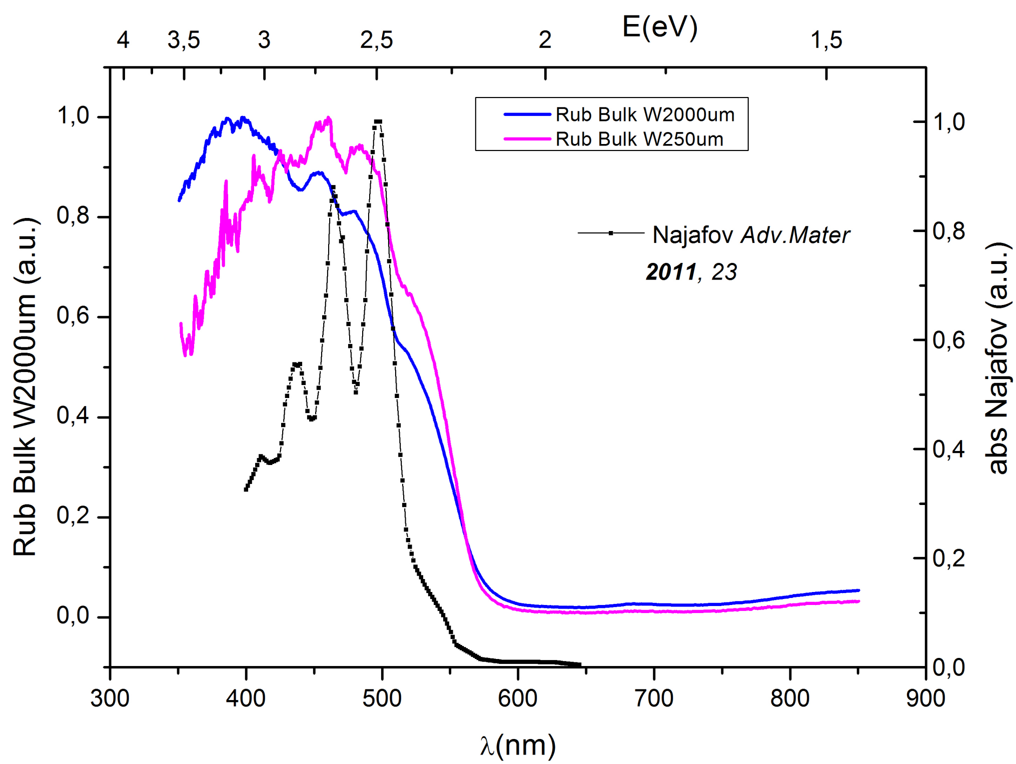

Figure 5.5: Comparison between photocurrent of rubrene bulk with two different slits and absorption spectra of [7]

Conclusions and Outlook

We have analyzed transport properties of rubrene single crystal in bulk and thin film forms, as FET and as free standing crystals. These properties were analyzed by means of the SCLC model and photocurrent experiment. By studying Rubrene single crystal thin films and bulk we found that the mobility increase with the film thickness. The thinner film has a thickness of 15nm and mobility of $9.5\dot{1}0^{-3}(cm^2/Vs)$ while whilethe rubrene bulk has a mobility about $2.1cm^2/Vs$. IV characterization of FET shows a hopping transport possibly due either to a strong contact resistance effect or to lattice mismatch with the substrates. The contact resistance is negligible at room temperature, and to confirm the role of lattice mismatch effect further experiments are needed with other substrates. From IV studies of thin films we determined that contact resistance is practically negligible at room temperatures, but we discovered a Schottky effects in a range from 280 to 2190K. After an annealing treatment on the metal electrodes fabricated on rubrene thin films, the Schottky effects disappear. From the annealed sample we extracted the electronic density of states distribution which has an exponential trend as expected and diminishing with temperatures increase. From photocurrent spectroscopy we extract an energy gap of 2.2eEV as reported in literature and that crystal order is confirmed for thinner to bulk samples, which presents peaks at the same energies. Further measurement need to be performed to better understand the small shift of photocurrent spectrum with respect to photocurrent reported in literature for macroscopical rubrene single crystal.

Bibliography

[1] N. Sato K. Seki H. Inokuchi T. Takahashi, Y. Harada and S. Fujisawa. Gas and solid phase photoelectron spectra of 5,6,11,12-tetra-phenylnaphthacene (rubrene). *Bulletin of the Chemical Society of Japan*, **52** (1979).

[2]

[3] D. Käfer and G. Witte. Growth of crystalline rubrene films with enhanced stability. *Physical Chemistry Chemical Physics*, **7** (2005).

[4] Q. Shi H. Fu J. Ma L. Huang, Q. Liao and J. Yao. Rubrene micro-crystals from solution routes: their crystallography, morphology and optical properties. *Journal of Materials Chemistry*, **20**(2010).

[5] M. L. Toh K. K. Zhang C. Kloc, K. J. Tan and Y. P. Xu. Purity of rubrene single crystals. *Applied Physics A*, **95**(2008).

[6] T. Siegrist D. V. Lang Woo-Young So O. Mitrofanov, C. Kloc and A. P. Ramirez. Role of synthesis for oxygen defect incorporation in crystalline rubrene. *Applied Physics Letters*, **91**(2007).

[7] E.Garfunkel L. Feldman V. Podzorov H.Najafov, D.Mastrogiovanni. *Adv.Mater.*, **23**, 2011.

[8] G. Weidlinger Sh.M. A. Al-Baqi-H. Sitter H. Zaglmayr, L.D. Sun and P. Zeppenfeld. Initial stage of crystalline rubrene thin film growth on mica (0 0 1). *Synthetic Metals*, **161**(2011).

[9] K. H. Lee-H. W. Yeom S. Im Se-Woong Park, Jeong-Min Choi and Y. K. Lee. Amorphous-to-crystalline phase transformation of thin film rubrene. *The Journal of Physical Chemistry B*, **114**(2010).

[10] P. Chiaradia A. Sassella C. Goletti, G. Bussetti and A. Borghesi. Highly sensitive optical monitoring of molecular film growth by organic molecular beam deposition. *Applied Physics Letters*, **83**(2003).

[11] A. Troisi. Prediction of the absolute charge mobility of molecular semiconductors: the case of rubrene. *Advanced Materials*, **19**(2007).

[12] R. M. Owens D. A. Bernards and G. G. Malliaras. *Organic semiconductors in sensor applications*. Springer Series in Materials Science,Springer London, Limited, (2008).

[13] I.Kymissis. *Organic Field Effect Transistors*. Springer, 2009.

[14] G.Horowitz D.Braga. High-performance organic field-effect transistors. *Adv. Mater.*, **21** (2004).

[15] T.M. Klpwijk A.F. Morpurgo J.Niemax-A.K. Tripathi J. Plaum R.W.I. de Boer, M.Jochemsen. *J. Appl. Phys*, **95** (2004).

[16] D.Braga *et al.* Bulk electrical properties of rubrene single crystals: Measurements and analysis'. *Physical Review B*, **77** (2008).

[17] H. Bouchriha R. Bourguiga M. Hajlaoui G. Horowitz, R. Hajlaoui. *Adv. Mater*, **10** (1998).

[18] N. F. Mott and R. W. Gurney. *Electronic processes in ionic crystals*. Clarendon Press, (1940).

[19] J.Swobakowski S.Nespurek. A differential method of analysis of steady-state space charge limited current-voltage characteristics. *phys.stat.sol (a)*, **41**(1977).

[20] S. Nespurek and J. Sworakowski. Use of spacechargelimited current measurements to determine the properties of energetic distributions of bulk traps. *Journal of Applied Physics*, **51**(1980).

[21] G. Borghs J. Reynaert, V. I. Arkhipov and P. Heremans. *Appl. Phys. Lett*, **85**(2004).

[22] C. Krellner. *Transport and Defects in Organic Single Crystals*. PhD thesis, (2004).

[23]

[24] J. Sworakowski S. Nešpurek, O. Zmeškal. Space-charge-limited currents in organic films: Some open problems. *Thin Solid Films*, **516**(2008).

[25] S. Nešpůrek O. Zmeškal, F. Schauer. *J. Phys. C. Solid State Phys*, **18**(1985).

[26] H.Aubin G.Horowitz P.Lang, M-Mottaghi. Extracting parameters from the current-voltage characteristics of organic field-effect transistors. *Advanced Functional Materials*, **14**(2004).

[27] F.Pascal M.J.Deen. Electrical characterization of semiconductor materials and devices. *J Mater Sci: Mater Electron*, **17**(2006).

[28] Richard Bube. *Photoconducivity of Solids*. Krieger Publishing Company, 1978.

[29] L.Basiricò. *Inkjet Printing of Organic Transistor Devices*. PhD thesis, 2012.

[30] L.E. Lyons F.Gutmann. *Organic Semiconductors*. Wiley, 1967.

[31] Q.Zhou L.Feldman V. Podzorov H.Najafov, B.Lee. *Nature Materials*, **9** 2010.